# Stability and failure modes of slopes with anisotropic strength: Insights from discrete element models

Marius Huber, Luc Scholtes, Jérôme Lavé

## To cite this version:

Marius Huber, Luc Scholtes, Jérôme Lavé. Stability and failure modes of slopes with anisotropic strength: Insights from discrete element models. Geomorphology, 2024, 444, pp.108946. 10.1016/j.geomorph.2023.108946 . hal-04331588

HAL Id: hal-04331588
https://uca.hal.science/hal-04331588v1

Submitted on 8 Dec 2023

**Title:**

# Stability and failure modes of slopes with anisotropic strength: Insights from discrete element models

**Authors:**

Marius Huber[1, 2, *], Luc Scholtès[3], Jérôme Lavé[1]

[1]Université de Lorraine, CNRS, CRPG, Nancy, France

[2]Université de Lorraine, CNRS, GeoRessources, Nancy, France

[3]Université Clermont Auvergne, CNRS, IRD, OPGC, LMV, Clermont-Ferrand, France

* corresponding author:

E-mail address: marius.huber@univ-lorraine.fr

Postal address: Centre de Recherches Pétrographiques et Géochimiques (CRPG)
15 rue Notre Dame des Pauvres BP 20
54500 VANDOEUVRE-LES-NANCY, FRANCE

## Abstract

This paper investigates the relationships between hillslope stability and fabric anisotropy of brittle rock materials and the implications for landscape shaping. We use discrete element models to study the stability and failure modes of slopes made of transverse isotropic rock materials, focusing more particularly on the influence of the material orientation relative to the topographic slope. After validating the numerical approach with a limit equilibrium analytical solution in the case of an isotropic material, we modify our numerical slope models to simulate the rheological features of anisotropic gneissic rocks. Systematic exploration of the transverse isotropy plane's orientation in two dimensions (dip angle) reveals that slope collapse requires strength values that are highly dependent on the orientation of the material relative to the slope. For a 1000 m high escarpment, the stability of a slope with a fixed gradient requires strength that is one order of magnitude greater in a configuration where the isotropy plane is slightly less inclined than the topographic slope (i.e., cataclinal overdip configuration) than in a configuration where the isotropy plane is perpendicular to the slope (i.e., anaclinal configuration). Mirroring this highly variable stability according to the relative orientation of the material, four modes of deformation or gravitational instability are observed: in order of appearance, when the transverse isotropy plane orientation goes from 0 to 180° with respect to the horizontal (going from cataclinal to anaclinal configurations), the slope collapses respectively by sliding, buckling, toppling and crumbling. The crumbling mode corresponds to a very stable configuration for which the preferred ground movements will be rock falls from the cliff compared to the structurally controlled, deep-seated deformation modes leading to sliding and toppling. Despite the simplifications inherent to the numerical approach, our study highlights the essential characteristics of landslides occurring along slopes cut in transverse isotropic materials and reproduces the various instability modes observed in natural slopes. It also enables assessing their respective kinetics as well as the volumes of material they mobilize. Finally, by comparing our findings on the azimuthal variations in hillslope gradients observed along the central Himalaya (Nepal), in an area characterized by the relatively uniform orientation of the anisotropy in gneissic and mica-schist formations, we show that, even though multiple environmental factors come into play, landscape shaping is indeed strongly controlled by material anisotropy.

**Keywords**

Slope stability, landslides, failure modes, rock, anisotropy, numerical modeling, discrete element method

## 1. Introduction

Landslides are known to play a key role in shaping landscapes (Densmore and Hovius, 2000; Korup et al., 2010) and are a major hazard for millions of people and infrastructure globally (Glade et al., 2005; Davies, 2021), especially evident nowadays in mountainous regions in times of global warming (e.g., Huggel et al., 2012). The study of their dynamics and the control by factors like climate, lithology, and tectonics on predisposing and triggering slope failures is fundamental for improving of natural disaster preparedness and better understanding of the Earth's surface evolution over time.

Among the factors governing slope deformation, geological structures, with their different forms related to nature and scale, are probably the most critical (Jaboyedoff et al., 2011; Stead and Wolter, 2015). Apart from large discrete structures such as folds, faults, and unconformities, intrinsic textural anisotropy is commonly present in many rocks near Earth’s surface through the lithology itself in the form of layering and/or foliation. This homogeneously distributed matrix anisotropy, that predominantly corresponds to transverse isotropy (TI), is not necessarily localized by bedding planes or joints, and usually concerns the entire rock mass. The ability of TI rock materials to deform and withstand stresses varies according to the orientation of stresses relative to their isotropy plane (Hoek, 1964; Barton and Quadros, 2014). Therefore, the orientation of a slope with respect to the plane of isotropy significantly affects its overall stability, particularly the rupture localization and the associated failure mode. Slope failures related to bedding planes, schistosity, or joint sets have been described and studied for either natural (e.g., Stead and Wolters, 2015) or engineered slopes (e.g., Read and Stacey, 2009; Cheng and Lau, 2014). For natural slopes, such failure characteristics should play a key role in shaping the landscape.

Indeed, topography associated with underlying inclined bedrock of layered or foliated rocks commonly features landforms described by geomorphologists as dip slopes, escarpments or homoclinal ridges (e.g., Cotton, 1949). Cruden and Hu (1999) and Cruden (2000), based on a theory that links bedding orientations to slope angles in sedimentary sequences of the Canadian Rocky Mountains, identified two major failure modes, sliding and toppling, respectively, and observed that slope angles decrease when the bedding is oriented parallel to the slope. Chigira (1992) identified different deformation patterns governed by the preferential orientation of structures relative to the slope morphology from analyses of slow-moving landslides in Japan. Chigira (2000) built upon these observations to define four distinct failure modes controlled by the relative orientation of the slope with respect to the bedding (or foliation), i.e., sliding, toppling, buckling, and a dragging mode for slopes that are principally stable but nonetheless subjected to a deep-seated deformation process with a rupture zone cross-cutting the bedding planes at depth. Grelle et al. (2011) also identified in southern Italy certain conditions strongly related to the bedding orientation with respect to the slope, susceptible to promoting landslides in a bedrock composed of an interlayering of clayey and stony sediments. Besides, studying landslides triggered by the 1933 Diexi earthquake in China, Cui et al. (2022) found variability in failure mode, frequency, and landslide-affected area as a function of lithology and bedding orientation relative to the slope. All these studies show that the mode of failure and the susceptibility of a slope to failure is strongly dependent on the orientation of material anisotropy, i.e., bedding, schistosity, or regular jointing.

Many rock-mechanical lab-scale tests have been performed on a variety of TI rocks worldwide to assess their direction-dependent properties (see e.g., Donath, 1961; Hoek, 1964; McLamore and Gray, 1967; Niandou et al., 1997; Nasseri et al., 2003; Bonnelye et al., 2017). All these tests show that strength properties and failure modes are highly direction-dependent in such rock materials. For instance, Tien et al. (2006) used compression tests on an analog rock material to illustrate how the failure mode and strength change depending on the isotropy plane inclination with respect to the principal stress. Transferring results from laboratory tests to the slope-scale requires scaling considerations (e.g., Brideau et al., 2009; Marinos and Carter, 2018) which makes assessing and characterizing the mechanical failure behavior of anisotropic rock media at the slope scale difficult. Existing studies with analog models can provide valuable insight into the behavior of slopes made up of regular pervasive joints: see, for instance, the centrifuge experiments that replicate flexural toppling (Adhikari et al., 1997) and sliding (Li et al., 2014), or the experiments with rigid blocks by Aydan et al. (1989). However, these studies remain descriptive, are performed only for a few joint orientations, lack scaling considerations for larger slope dimensions, and are technically challenging. It is, therefore, a logical step for scientists to resort to numerical methods to study anisotropic rock slopes, given their capacity to reproduce results systematically and to conduct comprehensive parametric studies, as well as the possibility they offer to set up geometries and loading procedures that could not otherwise be realized by analog experiments. Numerical studies of slope stability considering transverse isotropy are not so common in the literature. Some studies based on continuum approaches, included anisotropic rock strength in their model formulation for specific case studies (Agliardi et al., 2012; Roy et al., 2015; Wang et al., 2018) because it is unavoidable to take into account the direction-dependent strength of layered or foliated rock slopes. Azami et al. (2012) used the finite element method (FEM) to investigate the stability of a simple step-like geometry considering the full 180° range of angles possible in a slope made up of a TI material in two dimensional plane strain configuration. They determined the factor of safety for 22 different angular configurations and found two stability minima and two stability maxima when plotting their results against the full angle range. However, they did not use their methodology to track the temporal evolution or mode of failure in their simulations. Discontinuum approaches, thanks to their capability to explicitly describe discrete structures in materials, have been widely used for slope stability analysis and landslide research (see, e.g., the review by Stead and Wolter, 2015). These approaches, which apply either the discrete element method (DEM) (Cundall and Strack, 1979) or a hybrid method that combines the latter with the FEM (FDEM, Munjiza 2004) can describe large deformation typical of rock slope failures as well as their progressive failure (Wang et al., 2003; Utili and Crosta, 2011; Scholtès and Donzé 2012; Katz et al., 2014). They have been successfully used to investigate and reproduce complex failure mechanisms of historic landslides in anisotropic rock formations (see, e.g., case studies from Benko and Stead, 1998 and Zou et al., 2017), or to mimic and theoretically study step path failures of mono- or multi-modal pervasive joint sets inside rock slopes (Scholtès and Donzé, 2015; Zheng et al., 2018; Zheng et al., 2021; Sun et al., 2022). Nonetheless, despite their intrinsic capabilities and strengths over continuum methods, discontinuum methods have not yet been used to perform a valuable, comprehensive study covering the full range of possible rock strength anisotropy to slope face angles within rock slopes.

Here, we propose such an investigation to gain better insight into how anisotropy quantitatively affects slope stability and governs deformation characteristics and failure modes, aiming to shed light on how the TI rock orientation potentially modulates the Earth's surface topography and hazards in mountainous regions. First, we present our modeling approach and justify its relevance for simulating rock slopes and TI materials. Then, after comparing our model’s predictions to an analytical limit equilibrium solution that describes failure in isotropic slopes, we present a comprehensive study of TI rock slope stability that covers the full range of isotropy plane vs. slope orientation in two dimensions for two different slope gradients. The stability and failure modes observed over the entire range of orientations are then discussed, and a comparison is finally made with a satellite data extraction of the Annapurna Massif of Nepal to compare our findings in a natural setting.

## 2. Methods

### *2.1 The DEM model:*

To study rock slope stability, we used the discrete element method (DEM) implemented in the open-source software Yade Open DEM (Šmilauer et al., 2021). The rock material was simulated by spherical discrete elements (DE) bonded to one another through elastic-cohesive-frictional interaction laws governed by a modified Mohr-Coulomb criterion, as defined in the bonded particle model (BPM) of Scholtès and Donzé (2013) (see also Figure S1). In the present study, we built upon previous works dedicated to investigating slope stability using the same BPM (Scholtès and Donzé, 2012, 2015; Bonilla et al., 2015, 2017). The mechanical properties of the interparticle bonds dictate the overall emergent behavior of the DE assembly. The bonds can break to give place to purely frictional inter-particle interactions. Every time a bond breaks, a “crack” is defined at the former bond location. Cracks can be either of tensile nature (mode I) or of shear nature (mode II), depending on the local stress field. As classically done in the DEM, the simulations were calculated in iteration steps where the positions of the particles are updated based on an explicit time integration of Newton’s second law of motion. In addition, a non-viscous type damping was introduced to dissipate kinetic energy and favor the quasi-static nature of the simulated behavior. We used a damping coefficient of 0.5 for all the models presented hereafter (for details of the implementation, please refer to previously cited works and to Šmilauer et al., 2021).

### *2.2 Mode~~l~~ling anisotropic rock materials*

The BPM implemented in Yade has been recently enhanced to simulate TI rocks thanks to the introduction of isotropy planes at the scale of particle contacts (Dinç and Scholtès, 2018). Here, we make use of the same methodology to account for TI in our slope models (Figure 1a). Using the smooth contact logic proposed by Scholtès and Donzé (2012), preferentially oriented discrete weak bonds are introduced homogeneously within the particle assembly so that the overall emergent behavior presents the typical features of transverse isotropic materials, i.e., direction-dependent properties or anisotropic strength. As shown in Dinç and Scholtes (2018), the amount of these weak bonds and their mechanical properties have to be chosen carefully to ensure the simulated behavior is representative of the target rock material. In this study, we chose to simulate slopes made of a metamorphic rock. Following the procedure proposed by Dinç and Scholtes (2018), we thus calibrated our BPM to mimic the laboratory scale behavior of a gneissic rock presented in Saroglou et al. (2004). To do so, we performed a series of uniaxial test simulations (Figure 1b) and adjusted the BPM parameters to match the experimental behaviors described by Saroglou et al. (2004) with emphasis put on the direction-dependent strength properties characteristic of such rock type. As shown in Figure 1c, the calibrated BPM can reproduce the experimental observations: the uniaxial compressive strength evolves as a function of the angle $\theta$ between the principal stress direction and the isotropy plane with a typical asymmetric U-shape, the maximum strength corresponding to $\theta = 90°$ (loading perpendicular to the foliation), and the minimum strengths corresponding to $\theta \in [30°, 60°]$ (see the model properties in Table S1). Similarly, the Young modulus $E_{lab}$ of the simulated material varies with $\theta$, $E_{lab}$ being minimum for $\theta = 90°$, and maximum for $\theta = 0°$ such as $E_{lab}^{0°}/E_{lab}^{90°} \approx 1.5$, with $E_{lab}^{0°} \approx 55$ GPa. Of course, given our objective to simulate large rock slopes, we used a specific strategy to upscale these properties for our slope models (see Section 2.3.2).

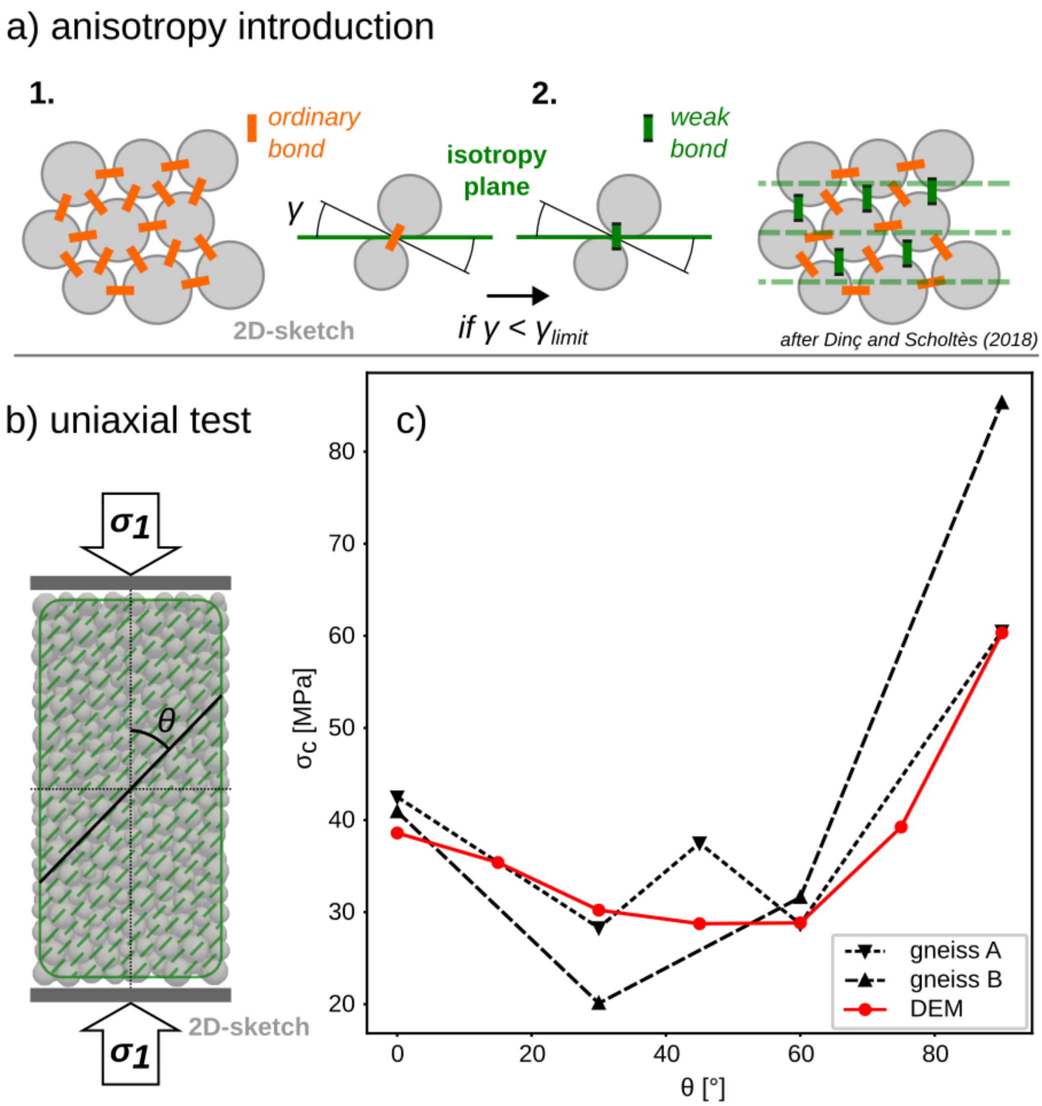

Figure 1: a) Selection (1) and reorientation (2) of ordinary bonds to preferentially oriented weak bonds in a DEM assembly to produce an emergent transverse isotropic behavior (after Dinç and Scholtès, 2018). γ is the angle used to detect contacts subparallel to the isotropy plane and to change the corresponding ordinary bonds to weak bonds. b) Uniaxial testing simulation used to calibrate the DEM model. θ is the angle between the isotropy plane and the major principal stress direction (axis of compression here). c) Comparison of the model prediction with the experimental observations by Saroglou et al. (2004): change in the uniaxial compressive strength as a function of θ.

Color in print, 1.5 column width

### 2.3 Model set-up

#### 2.3.1 Geometry, boundary conditions and preconditioning

Our slope failure experiments are performed on slope slices with a height of 1,000 m and a slope angle β that can be varied (Figure 2a-b). To avoid numerical artifacts caused by regular packings, the slope models were made up of particles presenting a polydisperse size distribution (with variation up to 1/3 of the predefined mean particle radius). The packings were generated through the progressive growth of particles initially randomly placed within a predefined closed volume (i.e., as a cloud of polydisperse particles). The growth was stopped when the porosity of the packing reached 30%, and the packing was mechanically stable. The mean particle radius was set to 20 m. The thicknesses of our slope slices are designed so that approximately 10 particles were present in the out-of-plane direction, a resolution that proved to give mesh objective results (see Section 3). Lateral boundary conditions were defined by blocking the translation in the direction normal to the boundary for the outermost particles (those whose centers are located within a zone of 3 times the mean particle radius from the boundary). At the bottom of the model, translations and rotations were blocked in all three directions for an equally defined layer of particles (Figure 2b).

To initialize stresses within our slope models, we adapted the loading procedure proposed by Katz et al. (2014), as illustrated in Figure S2. First, we applied gravity to a square packing of particles whose density $\rho_p$ was adjusted to ensure that the gravity-induced stress within the model corresponds to the stress found in a slope made up of a material with density $\rho$ = 2500 kg/m$^3$ (i.e., $\rho_p = \rho \cdot V/V_p$, with $V$ the volume of the model and $V_p$ the volume occupied by the particles). This gravity loading was performed considering 200 m of overburden above the final height of the slope. Then, after cutting of the overburden by eliminating particles from the simulation, the slope geometry was defined in a similar way by removing particles located above the final topography (Figure S2). This process was chosen to mimic the natural genesis of mountains where the subsurface is under the influence of the overlaying rock mass, and the topography only develops later through erosion, as observed for valleys forming through fluvial or glacial erosion in mountainous environments. The strength of all the interparticle bonds was set to a very high value during this preconditioning stage to ensure an elastic response of the model (i.e., no internal damage was induced up to the end of the preconditioning stage) (step 4 in Figure S2; Table 1).

2.3.2 Upscaled mechanical behavior

To define the properties of our slope models, we followed a procedure classically used in rock engineering where lab-scale properties are upscaled based on rock mass classification and associated empirical scaling indexes. For instance, the elastic properties of the slope models were defined following the approach by Hoek and Diederichs (2006), who proposed an empirical relation that relates the lab-scale Young's modulus of the rock material $E_{lab}$ to the rock mass deformation modulus E as a function of the Geological Strength Index (GSI):

$$E = E_{lab} \times \left(0.02 + \frac{1-D/2}{1+e^{((60+15D-GSI)/11)}}\right) \qquad (1)$$

where D is a disturbance factor related to the excavation method (we considered D = 0 here). The GSI is a rock mass classification index that relies on the description of rock structures and block surface condition, which can vary between 0 and 100 depending on the quality of the rock mass (Hoek et al., 2002). Originally built upon a large data set of field measurements, the GSI approach has been used successfully by geotechnical engineers for decades to upscale the mechanical properties of rock masses from lab-scale measurements. We used Equation (1) to define the elastic bond properties of our slope models based on the lab-scale values measured by Saroglou et al. (2004) and a GSI value ranging between 15 and 30 (see Table 1 for values). This GSI value would correspond to a moderately to severely damaged rock and could be assumed realistic for natural slopes affected by weathering and tectonism (Marinos and Hoek, 2000; Marinos and Carter, 2018).

In addition, we also altered the intrinsic strength of our slope models by adjusting the intR parameter of the BPM which is an explicit representation of the degree of particle interlocking (Scholtès and Donzé, 2013). At the lab scale, intR can be adjusted to simulate the behavior of more or less porous rocks, which would respectively present typical linear Mohr-Coulomb failure envelopes for intR = 1 or non-linear Hoek and Brown failure envelopes for intR > 1. Considering the scale of our slope models, the degree of particle interlocking can be seen as an indicator of the fracturing degree of the rock mass, and we thus made the choice to define intR = 1 in our simulations in order to take into account the role of defects of all sorts coexisting within the medium (faults, fractures, joints, etc.). Given the method that we used in our simulations, we don't have to define upscaled values for the strength parameters (see the following section).

### 2.3.3 Strength reduction method

Once the slope model is stabilized under gravity and the slope topography is cut, all bond strengths are initialized at the predefined values (see Table 1) and the actual simulation starts (Figure S2, step 4). The intrinsic model time is set to zero at this exact moment. The simulation consists of a strength reduction (SR) method that involves the progressive decrease of the interparticle bond strength, as proposed by Bonilla-Sierra et al. (2015). The tensile strength $T_p$ and the cohesion $C_p$ of the bonds (ordinary bonds only, since the weak bonds do not have any strength, as shown in Table 1) are reduced simultaneously to promote failure of the slope. The SR method enables to reach failure without having to predefine an upscaled strength for the rock material. Also, it provides critical strength reduction values at failure, which are case-dependent and thus enables assessing the proneness of different slope models to fail by comparing the amount of strength reduction needed to reach failure.

Practically, $T_p$ and $C_p$ decreased stepwise by 10% up to failure, the strength reduction factor (redFac) defining the cumulative reduction applied (see Figure S1 and Table 1). In this study, we combined different criteria to check if the slope models were stable and if further SR was needed (see Figure 2c-d). Practically, SR is applied if the three following conditions are met:

- the overall kinetic energy ($E_k$) remains below a threshold,
- a moving average of $E_k$, namely $\bar{E}_k$, remains below a threshold
- no cracks were generated since the previous checkpoint.

The redFac plotted over the iterations of a simulation allows us to determine the critical inter-particle strength needed for stability for each simulation (Figure 2c). For more information on the SR method, please refer to the Supplement (S1).

Table 1: Inter-particle bond properties of the slope models before SR is applied

| Parameter | ordinary bonds | anisotropy bonds |
|---|---|---|
| Interaction radius intR [-] | 1.0 | - |
| Elastic modulus Y [GPa] | 10 | 1 |
| Stiffness ratio P [-] | 0.1 | 0.1 |
| Tensile strength $T_p$ [MPa] | 100 | 0 |
| Cohesion $C_p$ [MPa] | 100 | 0 |
| Friction angle $\varphi_p$ [°] | 10 | 0 |
| Dilation angle $\psi$ [°] | - | 0 |
| Angle range $\gamma_{limit}$ [°] | - | 55 |

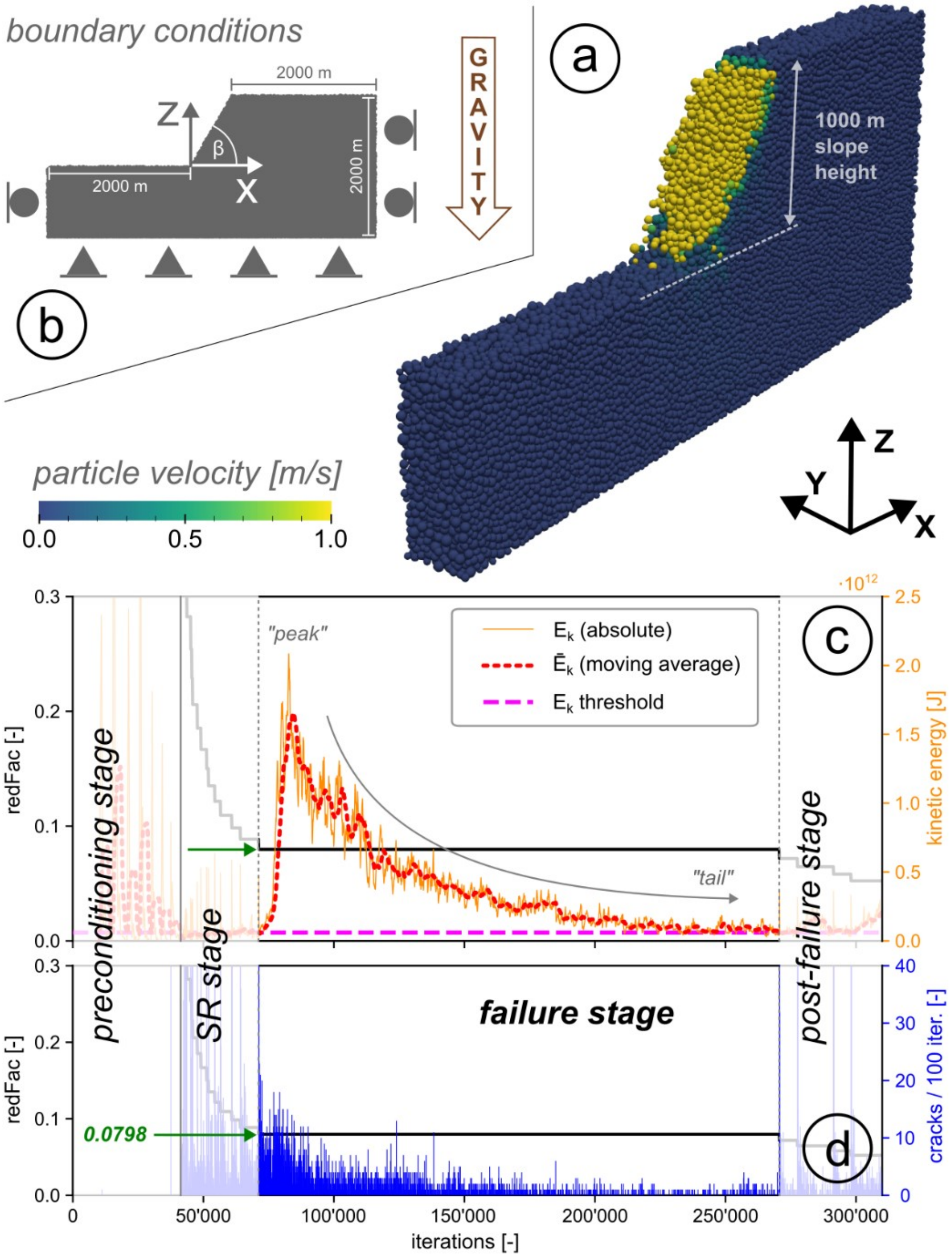

Figure 2: a) 3D view of a slope model at failure; b) boundary conditions; recordings from a simulation (anisotropy angle α = 70° and slope angle $\beta$ = 60°) that has been brought to failure by strength reduction (SR): c) reduction factor (redFac) and kinetic energy indices (absolute value $E_k$ and moving average $\bar{E}_k$), and d) crack frequency plotted over iterations.

Color in print, 1.5 column width

## 3. Relevance of the discrete element approach for investigating slope stability

Assessing the capability of numerical models to simulate slope failure in anisotropic materials is not straightforward. A recent study (Stockton et al., 2019) explores, using a semi-analytical procedure, the stability of slopes in the presence of frictional or cohesive anisotropy. However, the proposed definition of anisotropic cohesion as a $\sin^2()$ function of the angle between the isotropy plane and the principal stress direction is not consistent with our emergent TI behavior nor with uniaxial laboratory results for gneisses (Figure 1), so a direct comparison was not possible. We, therefore, preferred to assess the relevance of our numerical models by comparing their predictions with an analytical solution derived from stability analysis in the case of an isotropic material. We performed such a comparison considering the same geometry, loading procedure, SR method, and inter-particle bond properties as the ones presented in Table 1, except that no weak bonds were introduced into the model (see Section 2.2 and Figures 2 and S2). We compared our model results to the analytical solution derived by Leshchinsky et al. (1985) based on the limit equilibrium theory and a variational calculation scheme. The solution consists of a log-spiral failure geometry associated with a factor of safety (FoS) obtained for a slope step with a certain slope angle (β), made of a homogeneous Mohr-Coulomb (MC) type material with given cohesion (C) and friction angle (φ). It is thus possible to determine the critical MC strength properties (C, φ) of a slope and its rupture surface by considering FoS = 1.

The comparison exercise was also an opportunity to test the objectivity of the numerical model when varying some of its parameters, such as the number and size of its constitutive elements, their spatial arrangement, or the criteria used for the SR method. To this end, we carried out a total of 48 slope simulations on eight different packings built up with two different mean particle radii (R = 20 m and R = 15 m) and cut at two different slope angles β (40° and 60°). This parametric study showed that the results obtained are generally insensitive to the choice of particle radius or spatial arrangement, indicating that they are overall robust (see Supplement S2 for further details).

Table 2 summarizes the critical interparticle bond strength values ($C_p$ and $T_p$) and the corresponding emergent MC parameters at failure ($C_e$ and $\varphi_e$) obtained for the 48 slope simulations (see in Supplement S2 and S3 how these properties were obtained based on results of dedicated bi-axial tests, Figure S3). They are compared to the MC parameters predicted by the 2D solution of Leshchinsky et al. (1985). For both slope angles tested here, $\varphi_e$ ranges around 32°. For such a value of the friction angle φ, the analytical 2D solution predicts critical cohesion values C that are slightly different from the $C_e$ of the numerical material. Agreement on the cohesion values can be reached, however, by considering a slightly lower (around -2° offset) or higher (around 3° offset) friction angles for the 40° and 60° slopes, respectively. These minor deviations are nonetheless acceptable, taking into account the dispersion of the original $T_p$ and $C_p$ values (see Table S2) and the procedure used to obtain the emergent MC parameters (fitting a Mohr-Coulomb criterion to discrete values). Regarding the geometry of the failure plane, the numerical and analytical rupture surfaces are in close agreement for the $\beta = 60°$ slope simulations (Figure 3). For $\beta = 40°$, the analytical solution shows a slightly more pronounced curvature than the numerical solution (Figure S5). Overall, our numerical results compare relatively well with the analytical solution for both the MC strength parameters at failure and the geometry of the failure surface. We did not increment the slope height in our simulations because, according to limit-equilibrium description of slope stability problems (e.g., Leshchinsky et al., 1985), changing the slope height (e.g. to 100 m or 500 m) does not significantly change the geometry of the failure plane, but only changes the strength at failure by a proportionally inverse amount. For instance, for a slope height $H = 100$ m, we would simply get much higher $C_p$ and $T_p$ values at failure (see Figure 4) than for $H = 1000$ m with a similar rupture plane geometry, as predicted by the non-dimensional parameter $N = C/\rho g H$ (Leshchinsky et al., 1985), with material density $\rho$ and gravitational acceleration $g$.

Table 2: Comparison of DEM results and analytical solution after Leshchinsky et al. (1985). The DEM interparticle properties at failure correspond to means calculated over 4 different slope models run with different packings (see Table S2 in Supplement). The emergent MC parameters were obtained from back analyses of biaxial test simulations (see Table S2 in Supplement). The MC parameters at failure were obtained based on the 2D analytic solution (Leshchinsky et al., 1985) (values of interest in bold).

| | Topographic slope β = 40° | | Topographic slope β = 60° | |
|---|---|---|---|---|
| **DEM** | ***Interparticle strengths at failure*** | | | |
| | $\varphi_p$ [°] | $C_p$ & $T_p$ [MPa] | $\varphi_p$ [°] | $C_p$ & $T_p$ [MPa] |
| | 10 | 0.42 ± 0.13 | 10 | 2.86 ± 0.16 |
| | ***Emergent Mohr-Coulomb parameters*** | | | |
| | $\varphi_e$ [°] | $C_e$ [MPa] | $\varphi_e$ [°] | $C_e$ [MPa] |
| | 32 | 0.33 ± 0.03 | 32 | 1.14 ± 0.07 |
| **analytical solution** | ***Mohr-Coulomb parameters at failure*** | | | |
| | φ [°] | C [MPa] | φ [°] | C [MPa] |
| | 30 | **0.37** | 30 | 1.47 |
| | 31 | **0.31** | 31 | 1.40 |
| | **32** | 0.26 | **32** | 1.32 |
| | 33 | 0.21 | 33 | 1.25 |
| | 34 | 0.17 | 34 | **1.18** |
| | 35 | 0.13 | 35 | **1.11** |

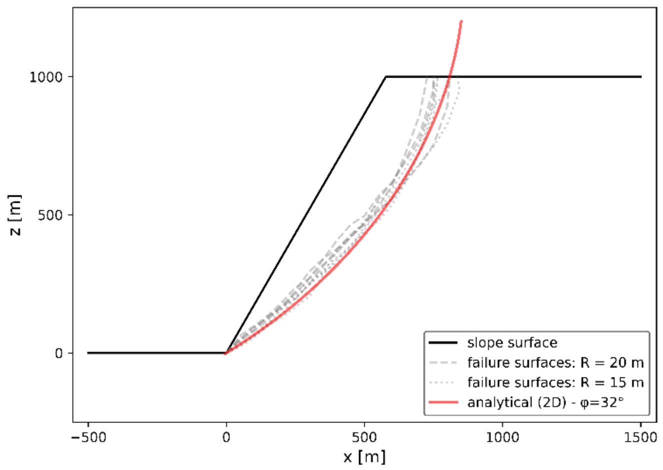

Figure 3: The $\beta$ = 60° slope results obtained for 2 resolutions (mean particle radius R = 20 m and R = 15 m respectively) compared to Leshchinsky et al. (1985)'s 2D analytical slope stability solution for φ = 32° (red curve).

Color in print, one column width

## 4. Results

SR simulations were conducted on two different particle arrangements, referred to in the following as packings P1 and P2, each with an identical mean particle radius of 20 m and the same overall geometrical properties but created from two different initial clouds of particles (see Section 2.3). We explored slope stability in two dimensions considering the full range of possible orientations of the isotropy plane relative to the horizontal (dip both towards and away from the slope, hereafter designated as the anisotropy angle $\alpha \in [0°, 180°]$, Figure 4) by running simulations every 10° increments considering two different slope angles ($\beta$ = 40° and 60°) for each packing.

### *4.1 Slope stability over the 180° range*

Overall, the $T_p$ and $C_p$ values at failure show similar trends for both the $\beta$ = 40° and 60° slopes, as well as strong variations depending on the angle $\alpha$ (Figure 4). As expected, 40° slopes fail for considerably lower inter-particle strengths, whatever the configuration (40° slopes are intrinsically more stable than 60° slopes). Slope models with an isotropy plane that rises less than the slopes themselves ($\alpha \in [130°, 170°]$), classified as cataclinal overdip slopes by Cruden and Hu (1996), fail with the highest $T_p$ and $C_p$ values, meaning that they correspond to the least stable slopes. The stability minimum $S_{min}1$ corresponds to $\alpha \approx 160°$. Slope models with isotropy planes dipping sub-vertically towards the slope ($\alpha \in [60°, 90°]$), defined as anaclinal slopes with steepened escarpment by Cruden and Hu (1996), fail for lower $T_p$ and $C_p$ values than $S_{min}1$ and show another stability minimum, $S_{min}2$, at $\alpha$ = 80°. Slopes with isotropy planes dipping at low angles into the slope ($\alpha \in [10°, 50°]$), classified as anaclinal slopes with subdued escarpment by Cruden and Hu (1996), fail for the lowest recorded inter-particle strengths, which means they correspond to the most stable slopes (for $\beta$ = 40°, interparticle strength values drop down to zero for some cases). For $\beta$ = 60°, the stability maximum $S_{max}1$ is at $\alpha$ = 20°. Another stability maximum $S_{max}2$ can be identified around $\alpha$ = 100°, a configuration that corresponds to cataclinal underdip slopes according to Cruden and Hu (1996).

By looking at the stability minima and maxima over the entire range of possible anisotropy angles, we observe an apparent symmetry over the $\alpha$ = 90° plane for both slope angles, with both minima and maxima lying 80° apart from each other.

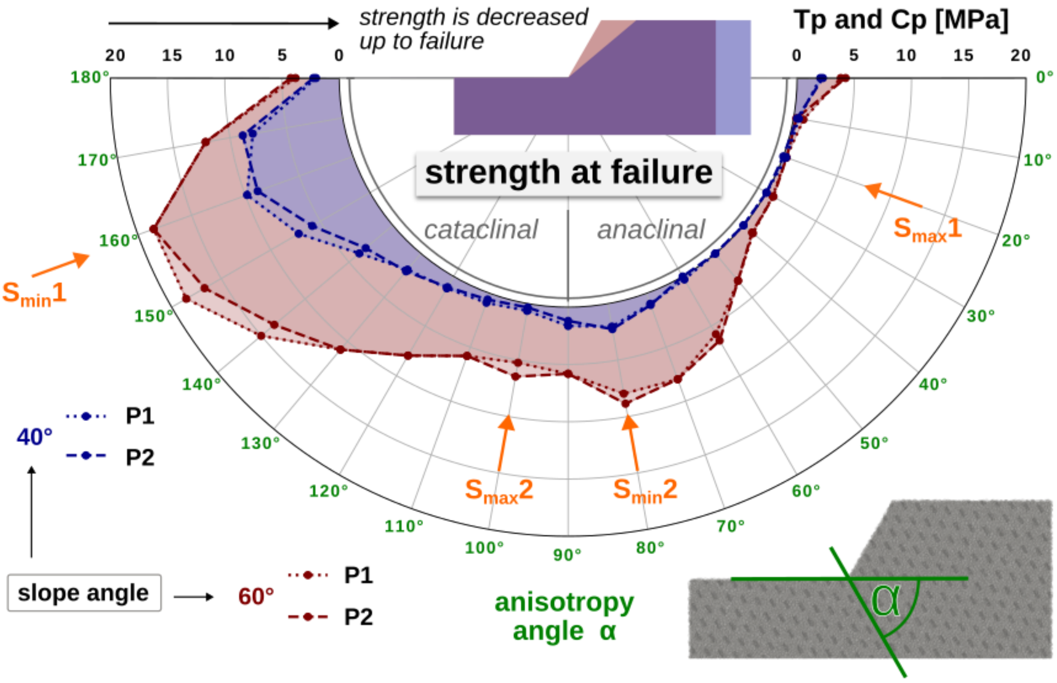

Figure 4: Stability curves over the full range of possible orientation (α) of the isotropy plane with respect to the horizontal: interparticle strength at failure ($T_p$ and $C_p$) obtained from DEM simulations performed on slopes with distinct angles (β = 40° and 60°). P1 and P2 are two different particle packings. Stability minima and maxima are indicated ($S_{min}$ and $S_{max}$).

Color in print, 1.5 column width

### *4.2 Stability extrema: overall kinetics*

Our simulation results can be further explored by comparing failure index parameters evolving (like in Figure 2, Section 2.3). Here, we only investigate the β = 60° slope angle simulations (packing P1) corresponding to the four stability extrema. In Figure 5, we plot out their respective critical strength values, $T_p$ and $C_p$, their overall kinetic energy $E_k$, and their accumulated total number of cracks over the simulation time. Only cracks occurring near the slope surface are accounted for in the analysis (see Figure S6). The plots reveal significant disparities in failure evolution for the four cases (the respective start and end of the failure stage are marked with vertical red lines in Figure 5a-d).

First, the more stable configurations (α = 20° and 100°) need more time/iterations to fail since they need more SR. For α = 100°, a minor instability is responsible for a small pre-failure plateau in the SR-curve (Figure 6c). $E_k$ does not rise high during this stage compared with the failure stage observed afterward, and we thus considered that this pre-failure stage was irrelevant when assessing the critical state parameters. This pre-failure stage resulted from the detachment of a few individual particles along the slope face that had to settle at the base of the slope before the SR could resume. For α = 20°, $E_k$ shows several peaks of low and similar magnitude, which were separated by periods of additional SR (see Figure 6d). The principal slope failure was assigned over all three SR plateaus as a multi-step failure (in Figure 4, $T_p$ and $C_p$ at failure were plotted for the lowest plateau in simulations where multi-stage failure occurred). The other three configurations display pronounced individual peaks of $E_k$ that differ in shape and magnitude (Figure 5a-c). The α = 160° configuration shows the highest rise in magnitude, but the peak has a short tail. The failure duration correlates directly with the length of the $E_k$-peak's tail. The α = 100° and α = 80° configurations need more time to stabilize after failure initiates compared to the α = 160° configuration. The latter configuration exhibits the smallest amount of cracks accumulated before and at the end of failure among all simulations. The α = 20° case already has a very high number of total cracks before its first failure and a low gradient of the cracks-curve during the failure plateaus (see Figure 5d). This can be explained similarly to the α = 100° pre-failure plateau by the detachment and subsequent fall-down of isolated particles. In contrast, the other simulations reveal much more intensified cracking during failure (Figure 5: steeper gradient of cracks-curve reflects intensified cracking within the slope).

The slope failure evolution is additionally tracked by making use of marker particle recordings shown in Figure 5e-h and Figure S7. They indicate fundamental differences in the way deformation takes place within the slope. For α = 160° they show a coherent translation of the elements along the slope surface far into the failure process (Figure 5e and Figure S7a). In contrast to the lower marker particles, the upper two marker particles have already subsided by several meters before the main failure sets in (Figure 5e). The marker particles of the α = 100° case (Figure 5f and Figure S7b) reveal that the mid-slope section (marker particles no. 2 and 3) drops down earlier than the lower part of the slope (marker particle no. 4). The lower two marker particles of the α = 80° case start to move a bit later but more suddenly and then faster than the upper two (Figure 5g and Figure S7c). For all simulations shown in Figure 5e-g, marker particle no. 4 (red line), which is located at the base of the slope, does not fall down consistently like the other marker particles located further upslope. For simulations with sub-vertically dipping isotropy planes (α = 80° and α = 100°), the drop of marker particle no. 4 slows down significantly. Overall, the marker particles of α = 80° and α = 100° (Figure 5e-f) move less uniformly than the ones of the α = 160° case (Figure 5g; see also Figure S7).

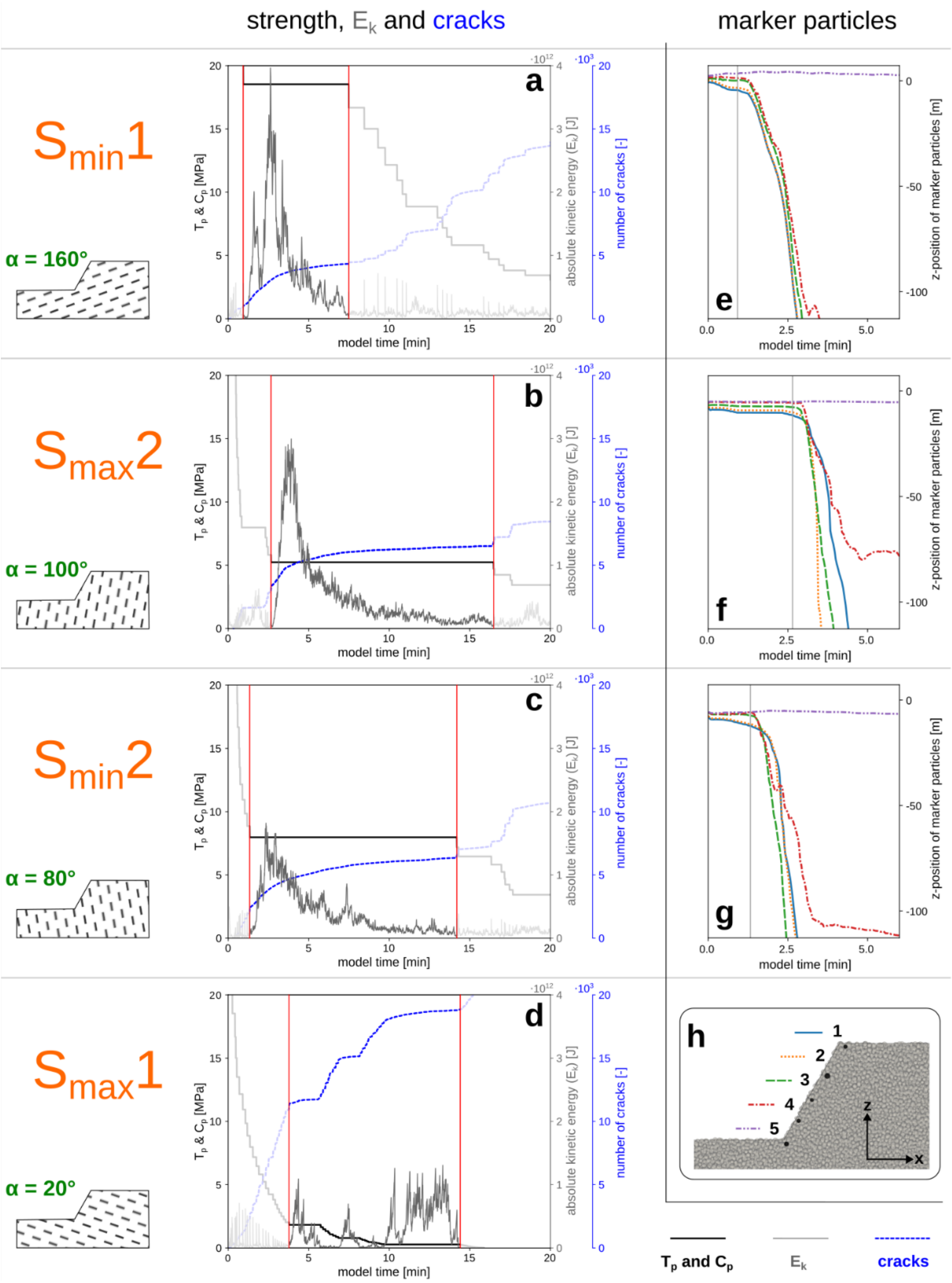

Figure 5: Failure characteristics of the four stability extrema observed for the β = 60° slope (packing P1). a - d: interparticle $T_p$ and $C_p$ reduced by SR method, absolute kinetic energy $E_k$, and cumulative number of cracks. Start and end of the main failure stage are indicated with red vertical lines. e - g: time records of the marker particles vertical position relative to their initial position; the vertical grey line indicates the start of failure; h: initial locations of marker particles on the slope.

Color in print, double column (full width)

*4.3 Stability extrema: failure behavior*

The deformation processes of the four anisotropy angles that yield extreme $T_p$ and $C_p$ values at failure for β = 60° are illustrated in Figure 6. The deviatoric strain maps (Supplement S3; Catalano et al., 2014) are plotted for 2 states within the failure stage to examine the onset of failure and its progression throughout the slope. As an additional indicator of the deformation, the cracks (broken bonds) that have accumulated up until the respective deformation stages are also shown. In addition, we present so-called layer cake visualizations in which the particles are alternately colored according to the orientation of the isotropy plane to better illustrate the different failure behaviors at more advanced points of the simulation. Finally, we extracted videos using the layer cake visualizations of Figure 6 from the beginning to the end of the failure stage for some configurations (Failure videos in Supplement) and also displayed the final stage of the failure process, representing the displacement and the damage index of each particle (Figure S8).

The failure of the stability minimum $S_{min}1$ ($\alpha = 160°$) initiates in the lower half of the slope and progresses further up along a rupture zone that eventually reaches the top of the slope (Figure 6a-b). Cracks appear mostly in the zone of high deviatoric strain that predefines the post-failure rupture surface (thin white line). A quasi-translational failure is observed with a well-defined primary block that slides along the failure surface and a secondary block slightly tilted on the upper end of the mobilized volume (Figure 6c). Cracks (i.e., damage) are mainly localized along the failure surface, corroborating the formation of a blocky structure that slides down the slope. The sliding mass retains most of its original shape, including a large undeformed chunk in its upper part (Figure S8, a and e), and collapses with only a minimal rotation during failure. The dip of the rupture surface is slightly steeper than the dip of the isotropy plane; thus, the rupture cuts across the isotropy plane.

The mode of failure observed for $\alpha \in [130°, 170°]$ is sliding. The Failure videos show that the internal deformation at the early stages of failure is much higher for $\alpha = 130°$ and gets lower with the shallower dipping angle at $\alpha = 160°$ where big parts of the sliding mass remain coherent, and deformation localizes mostly on the rupture surfaces. For $\alpha \in [150°, 170°]$, failures involve high mobilized volumes and the lowest amount of cracks among all the cases (Figure S9).

Figure 6 reveals that failures observed for $\alpha = 80°$ and $\alpha = 100°$ develop clearly differently than for the sliding case ($\alpha = 160°$): both of these simulations with subvertical isotropy planes show similarities as shown in the strain deviator maps. However, deviatoric strains and cracks observed for $\alpha = 80°$ tend to initiate only at the base of the slope, while for $\alpha = 100°$ they appear on almost the entire slope from the beginning (Figure 6c+e). For both cases, deformation is moving retrogressively towards the top and into the slope, soon affecting the entire slope and eventually defining the final rupture surfaces (Figure 6d+f). Many more cracks in the deeper subsurface formed for α = 80° and α = 100° compared to α = 160° since the SR at failure is more advanced (see Figure 4). The layer cake visualization for α = 80° shows a clear bending or toppling of the material in the vicinity of the slope face (Figure 6k), whereas the slope material appears to buckle with more particles detaching from the slope surface for α = 100° (Figure 6j). For both configurations, the entirety of the slope is strongly affected by deformation, as corroborated by the high density of cracks within the slope. The fact that almost the entirety of the failed material is severely damaged after the main failure in these cases (Figure S8f+g) indicates that failure occurs more diffusely compared to the blocky movement observed for α = 160° (sliding). However, the toe of the collapsed mass is located at a similar distance for the three configurations (Figure S8, a-c and e-g), likely controlled by the residual friction angle of the loose elements (see also Katz et al., 2014).

All simulations with α ∈ [60°, 80°] fail in toppling or bending mode. At the onset of failure, a large portion of the slope tilts and rotates towards the toe of the slope before the material subsequently disintegrates. The failure mode obtained for α = 90° is not that clear, and it can be considered transitional between the toppling and buckling failure modes. Despite a slight buckling movement that can be spotted in the lower half of the failing slope, the rotational movement ultimately prevails, and we classified this failure as toppling (see Failure video α = 90° in Supplement). Buckling is the mode of failure observed for all simulations with α ∈ [100°, 120°]. For all these cases, the material is bulging towards the surface in the lower half of the slope, followed by a rotational movement and severe break-up (hereafter referred to as buckling).

The shallow dipping, most stable configuration with α = 20° indicates a high amount of cracks even before the SR stops for the first time (see Figure 6g and compare with Figure 5d). The failure stage initiates with some superficial deformation detected in the upper part of the slope that likely corresponds to a few particles detaching. At a later point, the deviatoric strain is high along most parts of the slope surface, but, as shown in Figure 6h, failure does not propagate further within the slope. The deviatoric strain at the surface of the slope (Figure 6h) results from the detachment of a thin layer of particles which fall down the slope face, as illustrated in the layer cake visualization (Figure 6l), and tend to accumulate at its toe (see also Figure S8d+h). Interestingly, although no clear overall failure could be observed, extensive damage developed and spread over the entire slope, as evidenced by the high density of cracks within the medium. This extensive and deeply distributed damage was much more pronounced than in the other three extreme configurations, and the slope remains stable overall. Marker particles of the α = 20° case do not indicate relevant movements and were not presented.

The subdued anaclinal slopes with $\alpha \in [0°, 50°]$ fail in a mode that is best designated as “crumbling” (see Figure 6l and Failure video for α = 20° in Supplement). The transition from crumbling to toppling mode is unambiguous (compare Failure videos α = 50° and 60° in Supplement). This failure type observed in the most stable slope configurations is characterized by the detachment of individual particles on the slope face and, in the case of α = 50° and $\alpha \in [0°, 10°]$, by an advancing front of material disintegration from the slope face into the slope. Neither large-scale deformation before complete disintegration nor deformation acting deeper within the slope are visible for all the subdued anaclinal slopes. In Figure S9, we observe that some of the crumbling failures produced for α = 20°, 30° and 40° involve very low mobilized volumes: basically, only the surface layer of particles crumbles down the slope. However, of all the simulations, the crumbling failures show the highest number of cracks in the vicinity of the slope face (Figure S9).

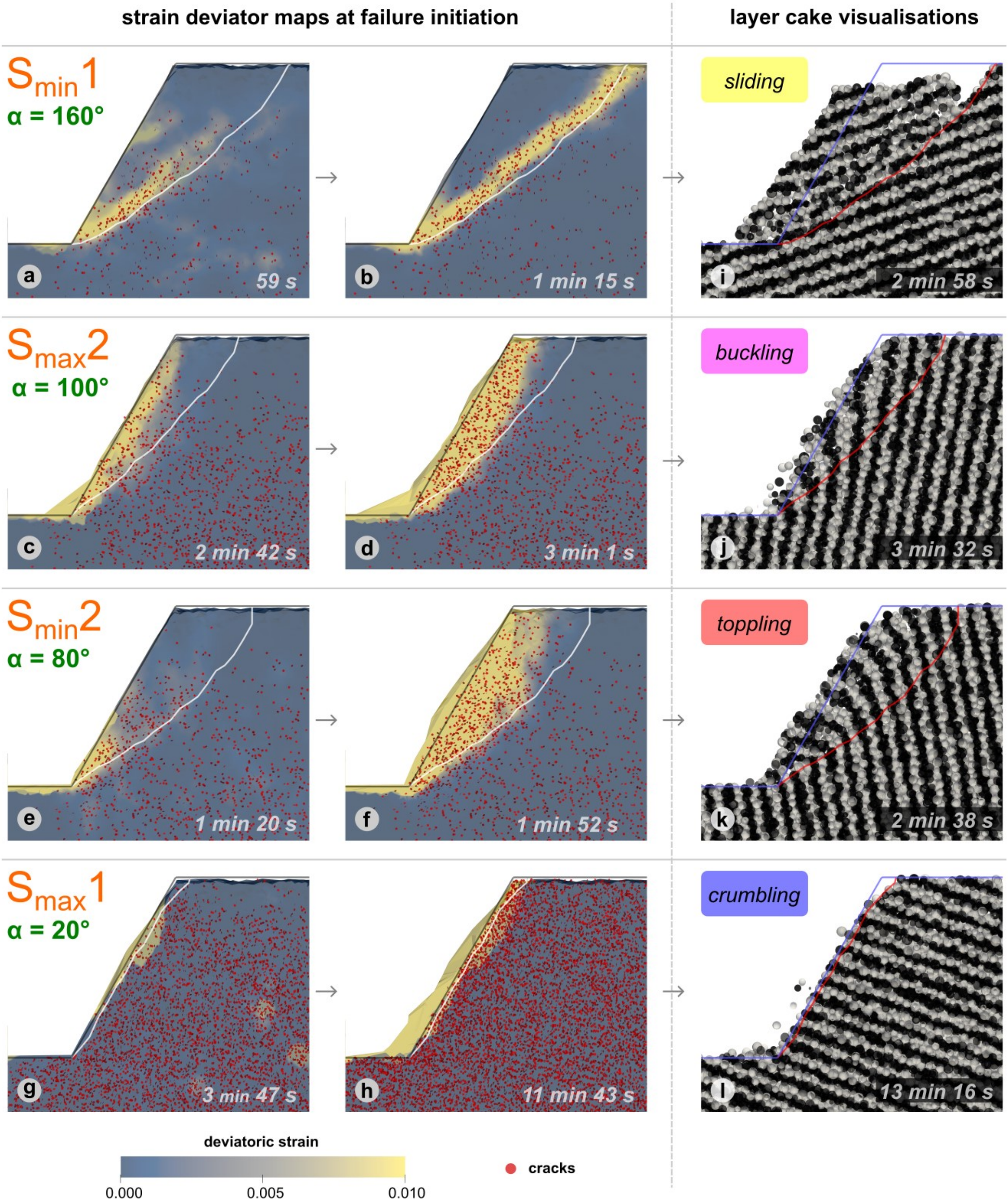

Figure 6: a - h: strain deviator maps (Supplement S3) with cracks at two early recording steps for the four stability extrema cases (β = 60°, packing P1). Black lines show original slope surface, white lines show rupture surfaces (Supplement S3). c - l: layer cake visualizations where layers are oriented according to the isotropy plane, final rupture surfaces here in red.

Color in print, double column (full width)

## 5. Discussion

Our modeling results correlate relatively well with findings from former studies that have investigated a partial (Sun et al., 2022) or the full (Aydan et al., 1989; Azami et al., 2012) range of possible strength anisotropy orientations relative to the slope. In comparison to these studies also covering the full range of possible anisotropy angles, our DEM approach enables us to record the failure initiation and progression for the first time in great detail. We confirm the previous results of Azami et al. (2012) concerning stability variations according to the relative orientation of anisotropy, and go further by describing four distinct failure modes with respect to deformation characteristics, estimates of mobilized volumes and damage potential (number of cracks), as well as analyses of the kinetics of failure in both space and time (please refer to Figures 4, 5, 6, S7, S8, S9). Overall, the configurations affected by sliding and toppling are the less stable ones, and the stability of each particular configuration is related to its failure mode (Aydan et al., 1989; Sun et al., 2022).

### *5.1 Modes of failure*

The stability extrema generated by our numerical approach correspond to four different modes of failure that can be differentiated by initiation, localization, type, and progression of deformation within the slope (Figures 5, 6, and S9): sliding (α = 160°), toppling (α = 80°), buckling (α = 100°) and a type of crumbling failure (α = 20°). Exploring the TI orientation for the entire 180° α-range (see also Failure videos in Supplement), it further appears that the failure mode can always be described by one of these four end-members (Figure 7). These anisotropy-induced failure modes are different from the circular failure mode observed in isotropic slopes (Figure S10 and compared with Figure 3).

The sliding and toppling modes observed for the least stable configurations are very well known and described in natural and engineered slopes with cataclinal overdip configuration or anaclinal slopes with steeply dipping layering, foliation or, joint sets (steepened escarpment), respectively (Hungr et al., 2014; Stead and Wolter, 2015). Buckling failure has been described in previous works for cataclinal slopes (e.g., Yang et al. 2020) but appears less frequently observed than the other two failure modes. Cruden (2000) also observed these three distinct failure processes (sliding, toppling, and buckling) on slopes in sedimentary rock masses in the Canadian Rockies, with buckling associated only with cataclinal dip slopes.

The crumbling mode, observed in our modeling for the highly stable shallow-dipping anaclinal configurations (subdued escarpment), has not been described as such in previous studies. However, Chigira (1992) described four modes of failure for slow-moving rock structures made up of different rock-types in Japan that are largely controlled by their host rock bedding or foliation angle. Besides the three modes of sliding, buckling, and toppling that match very well with our findings, he observed that anaclinal slopes with shallow-dipping TI angles are either stable or fail in a "dragging" mode. This dragging mode of failure is a localized, deep-seated, ductile, and slow-moving deformation that cross-cuts the bedding or foliation at a wide angle. According to Cruden (2000), when the bedding plane angle is favorable for neither sliding nor toppling, which corresponds roughly to $\alpha \in [0°, 50°]$ (for $\beta = 60°$), failures tend to follow or be guided by structural joints or fractures oriented orthogonally to the bedding plane. This switch to a secondary preferential structural plane of failure cannot be reproduced by our current model set-up, where only one isotropy plane exists, and localized deep-seated failures with a discrete fracture plane or rupture zone that cross-cuts the isotropy plane at a wider angle do not form. Instead, the corresponding slope models remain stable, implying the possibility for such configurations to present very high slope angles. In certain mountainous regions, such as the Canadian Rockies (Cruden, 2003), the angle of slope can indeed reach 65° in low cohesion rock masses for gently dipping bedding and anaclinal slope configurations, i.e., slope values well above the values of 35-40° usually observed in mountain ranges (e.g., Schmidt and Montgomery, 1995). In addition, at the bottom of such steep cliffs, it is quite common to observe talus deposition, produced by the accumulation of numerous rock falls, similar to the accumulation of detached particles observed in our modeling for the crumbling mode.

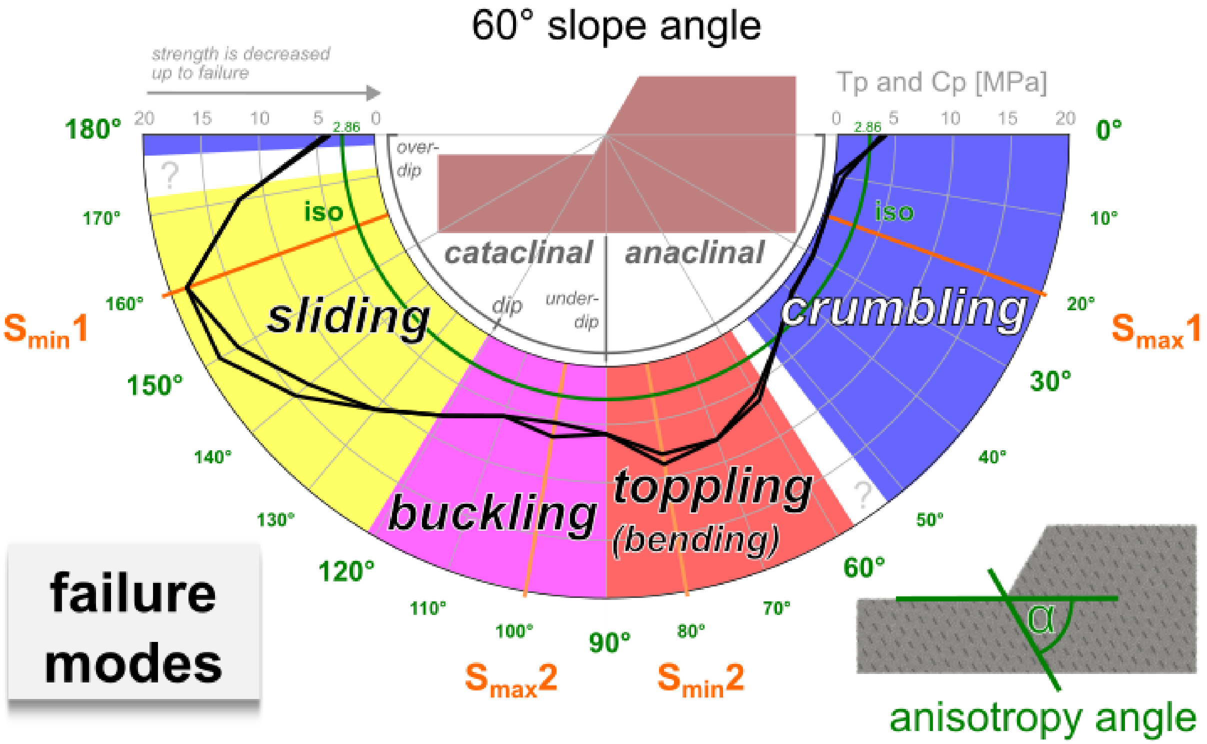

Figure 7: Failure modes observed for the β = 60° slope models depending on the orientation (α) of the isotropy plane with respect to the horizontal. See Figure 6 for layer cake visualizations of extreme stability configurations ($S_{min}1$, $S_{min}2$, $S_{max}1$, $S_{max}2$) and the associated Failure videos in Supplement.

Color in print, double column (full width)

*5.2 Mechanical interpretation*

The DEM set up enables us to extract the magnitudes and orientations of stresses acting on the particles that make up the slope (see Catalano et al. (2014) for details of the calculations). The magnitude of the differential stress ($\sigma_1$ - $\sigma_3$) and the orientation of the principal stress ($\sigma_1$) for all particles in the vicinity of the slope face are plotted together for both the stability extrema and the isotropic case in Figure 8 just before their respective main failure initiates. They can be directly related to the dimensionless failure potential $\Phi$, a measure of the potential for shear failure to occur adapted from Moon et al. (2017) and defined (Iverson and Reid, 1992):

$$\Phi = \left|\frac{(\sigma_1 - \sigma_3)}{(\sigma_1 + \sigma_3)}\right| \quad . \qquad (2)$$

Looking at the stresses within the isotropic slope model (Figure 8), it is evident that failure occurs in the region where $\Phi > 1$. This is much less evident for the anisotropic slopes because of the varying relation between stress orientation vs. isotropy plane orientation, and the direction-dependent shear strength (Fu and Dafalias, 2011).

In the overdip configuration failing in the sliding mode of $S_{min}1$ ($\alpha = 160°$), the isotropy plane is oriented favorably for the development of a shear zone oriented subparallel to it, as evidenced by the distribution of $\Phi$ within the slope (Figure 8). Moreover, the principal stress tends to be slightly tilted toward the direction of the isotropy plane, thus favoring stress concentration along this direction.

When the isotropy plane dips deeper than the slope face, the material cannot fail anymore through sliding along the isotropy plane, and slope stability increases substantially (Figures 4 and 7). For $\alpha$ = 100° ($S_{max}2$), $\Phi < 1$ in most parts of the slope except along the slope face, and the principal stress is subparallel to the isotropy plane. This stress distribution favors transverse buckling, which initiates at the base of the slope, where the compressive stress is higher, and progresses upward as a result of the progressive material excavation (Figure 6).

For toppling failures occurring in anaclinal slopes with steepened escarpments ($\alpha \in [60°, 90°]$), our results tend to verify the criterion proposed by Goodman and Bray (1976), assuming an emergent friction angle of $\varphi \leq \sim 30°$, which seems realistic in consideration of our analysis of the emergent mechanical properties of the DEM models (Section 2.3.2, Figure 7). In these configurations, toppling initiates as a result of shearing/sliding along the isotropy planes at the bottom half of the slope, as illustrated in Figure 8c for $\alpha$ = 80° ($S_{min}2$). There, contrasting $\Phi$-values seem to be localized preferentially along the isotropy planes. As for the sliding mode, the mobilized volume is bigger than for the isotropic case and corresponds to the area where $\Phi > 1$.

Unlike the sliding, buckling, and toppling failure modes, the crumbling failure mode corresponds to cases that are mostly more stable than the isotropic case (Figure 7). Why are the anaclinal subdued slopes so stable despite reducing the inter-particle strength substantially up to zero? According to Goodman and Bray's (1976) criterion, shearing/sliding cannot develop along the isotropy plane, and toppling cannot occur. Additionally, either circular or translational sliding failures would need shear zones to cross-cut the isotropy plane at a wide angle. Interestingly, the major principal stress ($\sigma_1$) of $S_{max}1$ ($\alpha = 20°$) does deviate more from the vertical than in the other extreme configurations, with $\sigma_1$ oriented almost orthogonally to the isotropy plane (Figure 8d), a configuration that would correspond to the highest strength configuration for TI materials (Figure 1). The slope finds itself in a "locking state” that promotes some sort of hardening of the material against failure (Figure 8d). One can notice that bands of higher $\Phi$ values are localized along the isotropy plane: given the orientation of these bands with respect to the slope geometry and, given the boundary condition on the right side of the model, the overall slope failure toward the left is impeded and only superficial material disintegration occurs along the slope face (i.e., crumbling). Even if we might question the role of bond reorientation (intrinsically linked to the introduction of anisotropy into our model, Figure 1a) in this hardening phenomenon, we note that this increase in shear resistance for certain isotropy plane orientations relative to the principal stress direction is known both from numerical and analog shear tests (Fu and Dafalias, 2011; Tong et al. 2014).

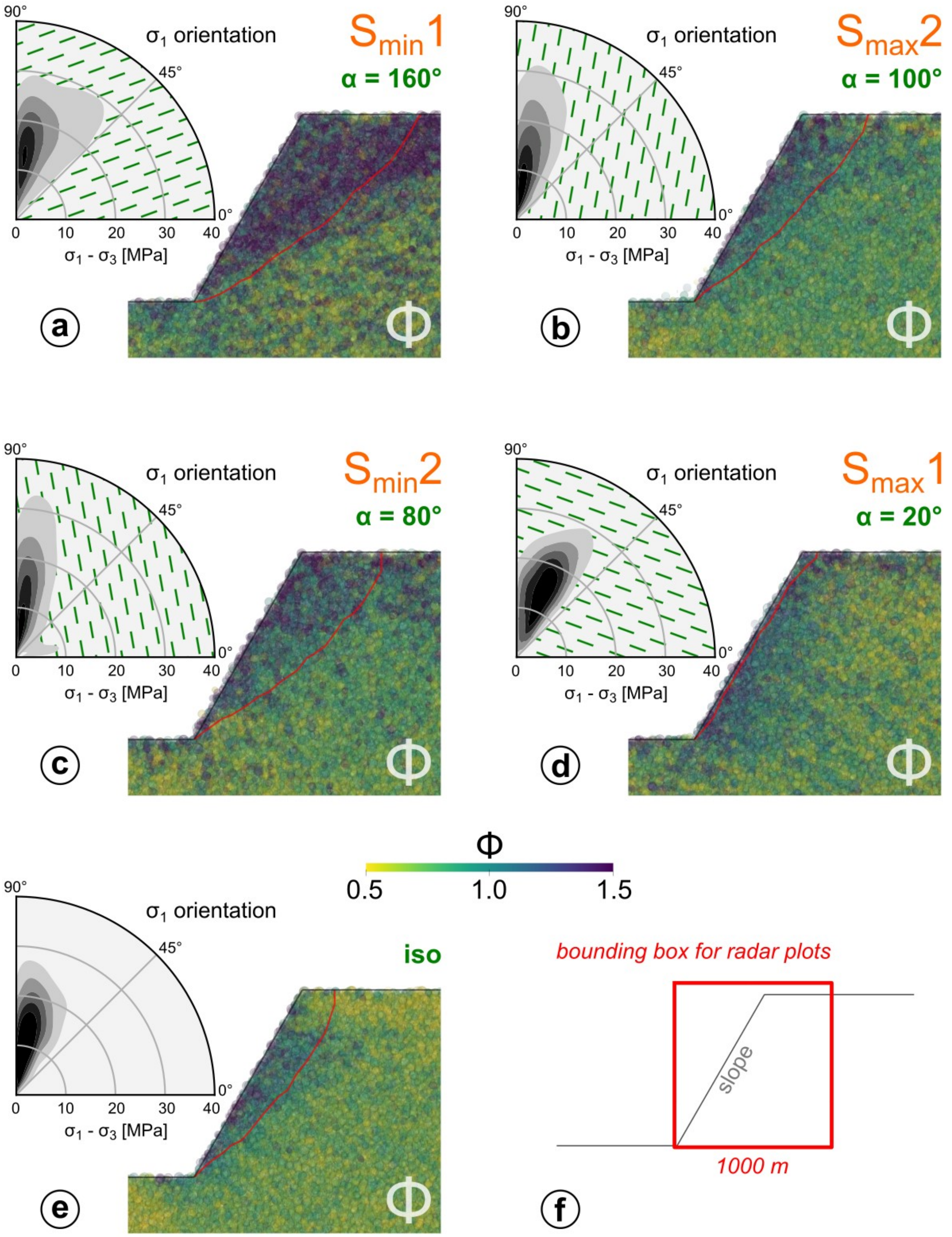

Figure 8: Stress distributions within the most representative slope models before failure: density plots show differential stress ($\sigma_1$-$\sigma_3$) plotted against principal stress orientation ($\sigma_1$) and slope visualizations show the dimensionless failure potential Φ. a-d: stability extrema with strength anisotropy, e: isotropic simulation, f: only particles in red box are used for the density plots.

Color in print, double column (full width)

### *5.3 Comparison with natural settings*

#### 5.3.1. How representative is our DEM approach?

To remain practical, a model designed to represent real-world phenomena must adopt simplifications to reduce the complexity of a natural environment. Natural slopes do generally comprise a lot of heterogeneities in the form of different lithological layers and discrete structures like joints, faults, and folds. Additionally, rock texture and strength may vary towards the surface and along discontinuities due to progressive fatigue and weathering processes (e.g., Brantut et al., 2013; Viles, 2013), and natural slopes often present complex topography that evolves gradually over time. All these ingredients that make every natural slope unique have a great impact on their mechanical behavior and, subsequently, on their failure process and mode. Our slope models do not account for geometrical and mechanical complexity. They are based on a simple step like geometry to be as general as possible and consider a diffuse material anisotropy rather than discrete structures in order to ease the consideration of scale effect and to avoid the explicit influence of only a few critical structures on the overall behavior. Despite their simplicity, our numerical simulations are capable to reproduce fairly accurate failure modes observed in natural settings that are controlled by rock strength anisotropy as shown, for instance, in studies focusing on landslides in Japan (Chigira 1992, 2000) or in the Canadian Rocky Mountains (Cruden and Hu 1996,1999; Cruden 2000, 2003). Strikingly, in their analysis of landslides triggered by the 1933 Diexi earthquake in China, Cui et al. (2022) found no rock topples but mostly rock slides on cataclinal slopes, and no rock slides but mostly rock topples on anaclinal slopes, which coincides well with our modeling results.

Furthermore, the presence of groundwater is known to be one of the most influential driving and triggering factors of slope failure due to the effect of pore pressure on the effective stress (Jaeger et al., 2007; Glastonbury and Fell, 2010; LaCroix et al., 2020). We do not account for groundwater in our modeling, and thus only consider total stress analysis under dry conditions, although it is well known that slope deformations are often related to short-term variations of pore pressures (Agliardi et al., 2020). The scaling we applied to derive realistic slope-scale mechanical properties based on the GSI approach was not initially designed for anisotropic rock masses (Marinos and Carter, 2018) and we are also aware that estimating GSI-values for large natural slopes is a complex undertaking (Brideau et al., 2009).

Another important aspect that distinguishes our simulations from natural slopes is the strength reduction method we applied. In our simulations, slopes are brought to failure by a homogeneous incremental decrease of strength up to a point where a small disturbance expands to a larger failure. Topography is already cut when SR sets in which does not correspond to the gradual evolution of slopes in natural settings. In nature, strength degradation does happen over time due to progressive weathering of bedrock, deepening of the front of alteration (e.g., Anderson et al., 2019), or stress fatigue induced by repeated seismic shaking (Gischig et al., 2016) or/and pore pressure increase (Petley et al., 2005; Agliardi et al., 2020). However, strength reduction within slopes is certainly not homogeneously distributed -either in space or in time as it is prescribed in our models. For this reason, it is difficult to transfer the temporal evolution of our simulated slope failures to natural slopes. Nevertheless, we observe some relative differences for failure duration between different configurations over the full range of possible isotropy plane orientations (α-angle) which might be of interest for field studies (see Figure S9c).

In our model results, the failure duration is minimal for the sliding mode, and double for the steeply dipping isotropy planes affected by buckling or toppling modes of deformation. It is difficult to assess the duration of failure of natural landslides. However, it may be asked whether anisotropic configurations and failure duration have an influence on the kinetic energy of the rock mass and on the mobility of the landslides. Similarly, could the differences observed between failure modes in the manner and speed at which failure propagates from bottom to top indicate differences in the type of instability? A reduced catalogue of DSGSDs in the Italian Alps (Ambrosi and Crosta, 2006) seems to indicate that these deep, progressive deformations develop more when the foliation of the rocks is relatively steep, i.e., when buckling or toppling are favored. At this stage, more exhaustive studies would be necessary, but the results of our study suggest a potential influence of the relative orientation of anisotropy on the overall dynamics of gravitational instabilities.

In concomitance with time scaling considerations, the transposition of our results to natural cases may require the addition of debris erosion in our modeling procedure. Indeed, as the collapse progresses, erosion of the debris base, particularly by a river, will modify the geometry of the debris apron and could promote the mobility of the collapsing slope. Future models dedicated to monitoring the temporal evolution of slope failure should consider erosion processes.

### 5.3.2 Rock anisotropy and hillslope angle at erosional steady state

In mountainous environments, as for any natural setting, strength reduction within slopes due to progressive weathering and fatigue of rock mass lead to a decrease of the resisting forces and therefore to hillslope instability. However, landslide triggering also is first of all driven by an increase of the tractive forces, i.e., the progressive increase of slope angle and relief. As tectonic processes uplift the land mass, rivers respond by incising their channel, thus lowering the local base level of the hillslopes: this leads to slope steepening and hillslope height increase until mechanical instability is reached. As denudation exhumes bedrock over time, the slope angles are therefore presumed to episodically adjust through landsliding, with an average angle that depends on the local bedrock strength (Townsend et al., 2020; Lavé et al., 2023). In the case of bedrock presenting TI characteristics (most sedimentary and metamorphic rocks), we expect the stability of slopes and average slope angles to vary significantly with slope orientations or slope aspects, as simulated by our study. In particular, anaclinal slopes should fail at higher slope angles than cataclinal slopes, as shown, for example, in Figure 4 for $T_p = C_p = 5$ MPa: for these fixed inter-particle bond properties, 60° sloping scarps developed in an anaclinal configuration are still stable, whereas the 40° sloping scarps developed in the overdip cataclinal setting have already failed. This expected result was indeed observed in the Rocky Mountains (Cruden, 2000). Although various earlier studies have looked at the relationship between the direction of anisotropy and slope orientation, they have mainly focused on the modes of failure (Cruden and Hu, 1996, 1999; Cruden 2000, 2003; Chigira, 1992, 2000; Teshebaeva et al., 2019; Cui et al., 2022) or on variations in landslide activity and frequency (Cruden and Eaton, 1987; Cui et al., 2022), but have paid, to our knowledge, little attention to the influence of this relative orientation on slope steepness.

To confirm that the anisotropy of the rock's resistance ultimately contributes to control the average slope angles in natural settings, we need to find a region where anisotropic structures are uniform at a scale larger than the typical hillslope length. Often, bedrock anisotropy is variable in an area due to folds, faults, and lithological changes, but in some places, the tectonic setting can result in large terrains of uniformly dipping unfolded rocks. Despite some minor secondary folding, this is the case for the south-facing slopes of the Annapurna Massif in central Nepal, where overthrusting due to continental collision is responsible for gneisses dipping consistently 10° - 40° towards NW - NE in between two major tectonic structures, the Main Central Thrust (MCT) and the South Tibetan Detachment (STD): see Figure 9a-b and refer to geological maps of Colchen et al. (1986) and Parsons et al. (2016). There, we performed a simple raster data analysis on a 30 m digital terrain model (Hawker and Neal, 2021) for an area high

2000 - 4000 m a.s.l. (red polygon in Figure 9a) actively eroding but devoid of any geomorphological evidence of hillslope glacial erosion and well below the permanently frozen areas where slope and rock mass cohesion are observed to be distinctively higher (Lavé et al., 2023). For the selected area, slope angle distributions appear to vary with slope orientation (Figure 9c): south-facing slopes are, on average, up to 9° steeper than slopes facing east, north, and west. Anaclinal slopes are, therefore, steeper than cataclinal slopes, as proven by our analysis (compare Figures 4 and 9). This finding agrees well with the observations of Uhlir and Schramm (1997) for central Himalayan slopes in a near-identical geological setting: constant dip of bedrock schistosity towards the north coincides with south-facing-slopes significantly steeper than north-facing slopes. The slope-aspect diagram in Figure 9c is qualitatively aligned with our modeling expectations if the variation in slope angle as a function of slope orientation is considered to be the cause of varying slope stability. However, a quantitative analysis of slope-scale mechanical conditions is difficult to perform at this stage, as it would be necessary to characterize the strength anisotropy of Himalayan gneisses, particularly at the scale of the hillslope (see Section 2.3). It would also be necessary to characterize slope stability when the azimuth of the isotropy plane is different from that of the topographic slope, i.e., we would need to numerically explore not only the dip angle of the isotropy plane in two dimensions but also its azimuth between 0 and 180° relative to the azimuth of the topographic slope in three dimensions. Additionally, the role of other factors, such as the distribution and orientation of fractures or the hydrology of groundwater, which is certainly influenced by stratified or foliated rocks (e.g., Dong et al., 2012), should be addressed.

As an additional corollary to this southern Annapurna slopes setting, we would expect, according to our modeling, differences in failure modes depending on the orientation of the slopes. Failures modes are difficult to assess by conventionally available satellite imagery due to rapid re-vegetation of landslide scars and the sparsity of large failures (>1 km2 landslides only occur every ~500 years following Marc et al. (2019)). Capturing a statistically representative frequency of the different failure modes for different slope orientations would require an exceptional number of slope failure events due to, for example, a very large earthquake (as in Cui et al. (2022) for the eastern margin of the Tibetan plateau), and/or the availability of a high-resolution digital terrain model (e.g., airborne Lidar). Despite the absence of such a quantitative approach, observations along the southern flank of the Himalayas (see Figure S11) are at least qualitatively in line with our model predictions. For instance, in the Ankhu Khola region (80 km to the east of the southern flank of the Annapurna Massif, in a near-identical setting), in conjunction with slope angle variability, slope failure modes are particularly contrasted between north-facing (cataclinal) and south-facing (anaclinal) slopes: low-volume rock falls, rock topples, and small rockslides appear to be more frequently observed on south-facing slopes, whereas numerous voluminous translational rockslides detach sub-parallel to the schistosity planes along north-facing slopes (Thouret, 1983; Uhlir and Schramm, 1997).

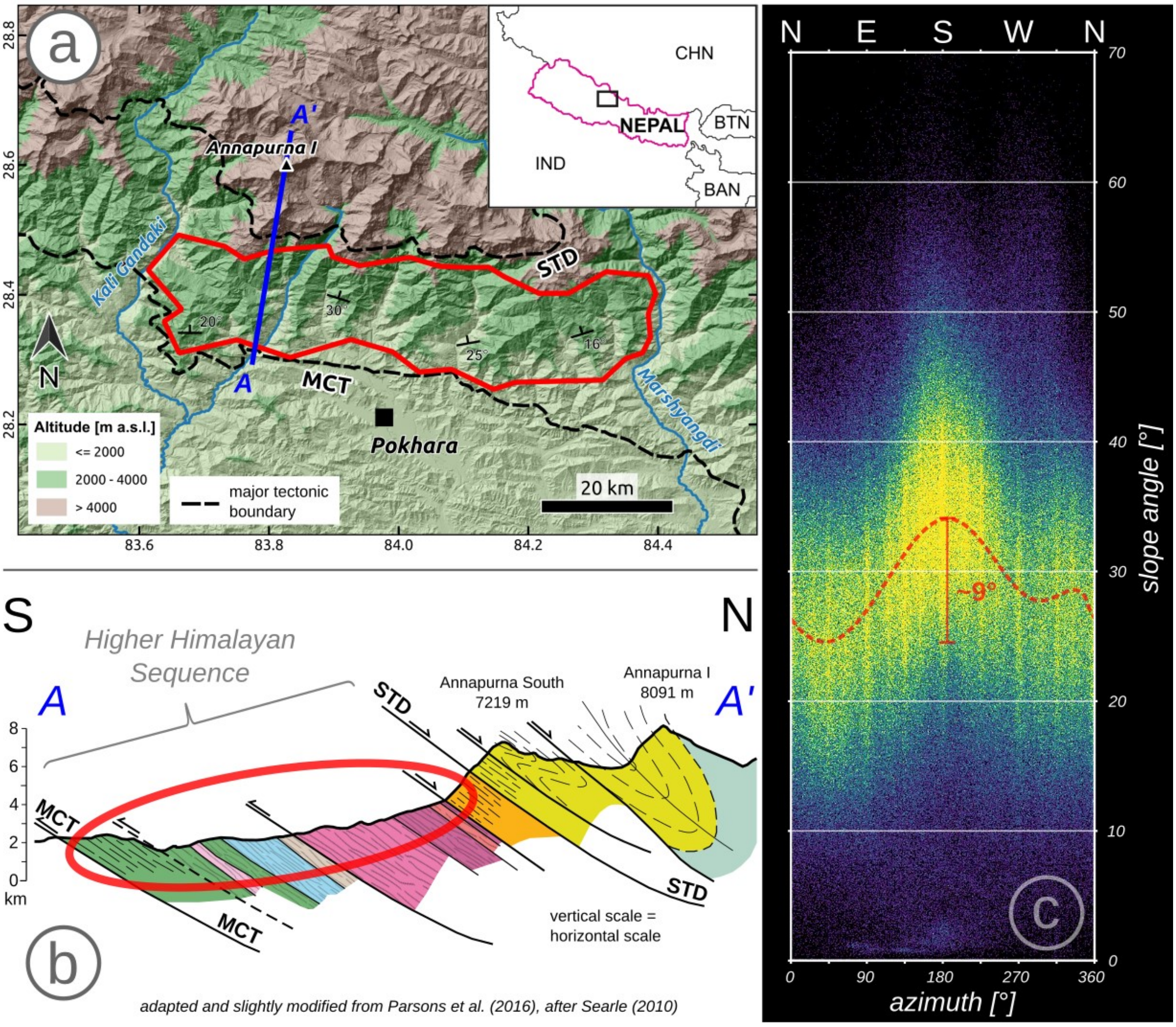

adapted and slightly modified from Parsons et al. (2016), after Searle (2010)

Figure 9: a: Topographic map of the Annapurna massif with location of area selected for raster data extraction (red polygon): country borders in white box (top left) serve as orientation, MCT and STD were extracted from the geological map of Parsons et al. (2016); b: tectonic profile modified after Searle (2010) (see location of blue line in a), red ellipse indicates terrain extracted for raster analysis; c) scatter plot showing azimuth - slope angle relationship colored by density (linear), red dashed line indicates the maximum density along azimuth.

Color in print, double column (full width)

## 6. Conclusion

Understanding the factors influencing the deformation and failure of rock slopes is fundamental to assessing slope failure hazard better and understanding landscape evolution. Using parametric numerical modeling, we explored the influence of rock anisotropy on slope stability, focusing more specifically on slopes made of transverse isotropic materials and investigating their stability potential and deformation modes. Our study enables us to identify distinct failure behaviors caused by different orientations of the isotropy plane with respect to the slope face, as regularly observed on natural and artificial slopes: sliding in overdip cataclinal slopes, toppling (bending) in anaclinal slopes with steepened escarpment, and buckling in underdip cataclinal slopes. One can also note that the crumbling failure mode does resemble rockfalls on anaclinal subdued slopes. Moreover, our approach enables us to relate the stability of slopes to these deformation modes. It suggests, for instance, that anaclinal slopes are generally more stable than cataclinal ones, with subdued escarpments showing the highest stability potential and overdip cataclinal slopes showing the lowest stability potential. Obviously, natural slopes exceed the bounds suggested by our modeling exercise due to their inherent complexity. Nonetheless, our results comprehensively describe all the first-order mechanisms that govern landscape evolution in mountainous areas where stability potential drives the topography. To go further into the analysis, one would need to include the contribution of additional factors to slope deformation, like pore pressure built-up or seismic shaking, that could greatly impact the prevailing failure mode and other failure characteristics. Nevertheless, our study, like that of Chigira (2000) on natural objects, indicates a whole typology of deformation modes that seem to depend directly on the presence of anisotropic rocks and on the relative anisotropy orientation with respect to the topography. It is difficult to know whether other factors may also lead to the emergence of the four identified end-members or whether the orientation of the anisotropy is the sole source of this typology. In any case, slope stability analyses should consider this parameter more systematically so that the various possible deformation modes and associated hazards can be clearly identified.

## Acknowledgements and Funding

We thank M. Zakari very much for his help in handling computing environments. Additionally, we would like to thank Sam McColl and one anonymous reviewer for inspiring and thorough reviews which helped improve our article. This study was funded by the Université de Lorraine (AMI Future leader grant) and Otelo program AAP interdisciplinaires. M. Huber's PhD grant has been funded by the Région Grand Est and the CRPG.

## Competing Interests

This research received no other external financial or non-financial support. There are no additional relationships, patents or additional activities to disclose.

## Declaration of generative AI and AI-assisted technologies in the writing process

During the preparation of this work the authors used the online AI-translator DeepL in order to improve the quality of the writing and to avoid translation errors. After using this tool, the author reviewed and edited the content as needed and take full responsibility for the content of the publication.

## References

Adhikary, D.P., Dyskin, A.V., Jewell, R.J., Stewart, D.P., 1997. A study of the mechanism of flexural toppling failure of rock slopes. Rock Mech Rock Engng 30, 75–93. https://doi.org/10.1007/BF01020126

Agliardi, F., Crosta, G.B., Frattini, P., 2012. Slow rock-slope deformation, in: Clague, J.J., Stead, D. (Eds.), Landslides. Cambridge University Press, Cambridge, pp. 207–221. https://doi.org/10.1017/CBO9780511740367.019

Agliardi, F., Scuderi, M.M., Fusi, N., Collettini, C., 2020. Slow-to-fast transition of giant creeping rockslides modulated by undrained loading in basal shear zones. Nat Commun 11, 1352. https://doi.org/10.1038/s41467-020-15093-3

Ambrosi, C., Crosta, G.B., 2006. Large sackung along major tectonic features in the Central Italian Alps. Engineering Geology 83, 183–200. https://doi.org/10.1016/j.enggeo.2005.06.031

Anderson, R.S., Rajaram, H., Anderson, S.P., 2019. Climate driven coevolution of weathering profiles and hillslope topography generates dramatic differences in critical zone architecture. Hydrological Processes 33, 4–19. https://doi.org/10.1002/hyp.13307

Aydan, Ö., Shimizu, Y., Ichikawa, Y., 1989. The effective failure modes and stability of slopes in rock mass with two discontinuity sets. Rock Mech Rock Engng 22, 163–188. https://doi.org/10.1007/BF01470985

Azami, A., Yacoub, T., Curran, J., 2012. Effects of strength anisotropy on the stability of slopes. Presented at the 65th Canadian Geotechnical Conference, CGS Geo-Manitoba.

Barton, N., Quadros, E., 2015. Anisotropy is Everywhere, to See, to Measure, and to Model. Rock Mech Rock Eng 48, 1323–1339. https://doi.org/10.1007/s00603-014-0632-7

Benko, B., Stead, D., 1998. The Frank slide: a reexamination of the failure mechanism. Canadian Geotechnical Journal 35, 299–311.Bonilla-Sierra, V., Elmouttie, M., Donzé, F.-V., Scholtès, L., 2017. Composite wedge failure using photogrammetric measurements and DFN-DEM modelling. Journal of Rock Mechanics and Geotechnical Engineering 9, 41–53. https://doi.org/10.1016/j.jrmge.2016.08.005

Bonilla-Sierra, V., Scholtès, L., Donzé, F.V., Elmouttie, M.K., 2015. Rock slope stability analysis using photogrammetric data and DFN–DEM modelling. Acta Geotech. 10, 497–511. https://doi.org/10.1007/s11440-015-0374-z

Bonnelye, A., Schubnel, A., David, C., Henry, P., Guglielmi, Y., Gout, C., Fauchille, A.-L., Dick, P., 2017. Strength anisotropy of shales deformed under uppermost crustal conditions. Journal of Geophysical Research: Solid Earth 122, 110–129. https://doi.org/10.1002/2016JB013040

Brantut, N., Heap, M.J., Meredith, P.G., Baud, P., 2013. Time-dependent cracking and brittle creep in crustal rocks: A review. Journal of Structural Geology 52, 17–43. https://doi.org/10.1016/j.jsg.2013.03.007

Brideau, M.-A., Yan, M., Stead, D., 2009. The role of tectonic damage and brittle rock fracture in the development of large rock slope failures. Geomorphology 103, 30–49. https://doi.org/10.1016/j.geomorph.2008.04.010

Cui, S., Wu, H., Pei, X., Yang, Q., Huang, R., Guo, B., 2022. Characterizing the spatial distribution, frequency, geomorphological and geological controls on landslides triggered by the 1933 Mw 7.3 Diexi Earthquake, Sichuan, China. Geomorphology 403, 108177. https://doi.org/10.1016/j.geomorph.2022.108177

Catalano, E., Chareyre, B., Barthélémy, E., 2014. Pore-scale modeling of fluid-particles interaction and emerging poromechanical effects. International Journal for Numerical and Analytical Methods in Geomechanics 38, 51–71. https://doi.org/10.1002/nag.2198

Cheng, Y.M., Lau, C.K., 2014. Slope stability analysis and stabilization: new methods and insight, Second edition. ed. CRC Press, Taylor & Francis Group, Boca Raton.

Chigira, M., 2000. Geological structures of large landslides in Japan. Journal of Nepal Geological Society 22, 497–504. https://doi.org/10.3126/jngs.v22i0.32423

Chigira, M., 1992. Long-term gravitational deformation of rocks by mass rock creep. Engineering Geology 32, 157–184.Colchen, M., Le Fort, P., Pêcher, A., 1986. Annapurna–Manaslu–Ganesh Himal. Centre National de la Recherche Scientifique, Paris 75–136.

Cotton, C.A., 1949. Geomorphology: an introduction to the study of landforms. John Wiley & sons, New York.

Cruden, D., Hu, X.Q., 1996. Hazardous Modes of Rock Slope Movement in the Canadian Rockies. Environmental and Engineering Geoscience 2, 507–516. https://doi.org/10.2113/gseegeosci.II.4.507

Cruden, D.M., 2003. The shapes of cold, high mountains in sedimentary rocks. Geomorphology 55, 249–261. https://doi.org/10.1016/S0169-555X(03)00143-0

Cruden, D.M., 2000. Some forms of mountain peaks in the Canadian Rockies controlled by their rock structure. Quaternary International 68–71, 59–65. https://doi.org/10.1016/S1040-6182(00)00032-X

Cruden, D.M., Eaton, T.M., 1987. Reconnaissance of rockslide hazards in Kananaskis Country, Alberta. Can. Geotech. J. 24, 414–429. https://doi.org/10.1139/t87-052

Cruden, D.M., Hu, X.-Q., 1999. The shapes of some mountain peaks in the Canadian Rockies. Earth Surface Processes and Landforms 24, 1229–1241. https://doi.org/10.1002/(SICI)1096-9837(199912)24:13<1229::AID-ESP42>3.0.CO;2-1

Cundall, P.A., Strack, O.D.L., 1979. A discrete numerical model for granular assemblies. Géotechnique 29, 47–65. https://doi.org/10.1680/geot.1979.29.1.47

Davies, T., 2022. Reducing landslide disaster impacts, in: Landslide Hazards, Risks, and Disasters. Elsevier, pp. 623–639.

Densmore, A.L., Hovius, N., 2000. Topographic fingerprints of bedrock landslides. Geology 28, 371–374.

Dinç, Ö., Scholtès, L., 2018. Discrete Analysis of Damage and Shear Banding in Argillaceous Rocks. Rock Mech Rock Eng 51, 1521–1538. https://doi.org/10.1007/s00603-017-1397-6

Donath, F.A., 1961. Experimental Study of Shear Failure in Anisotropic Rocks. Geol Soc America Bull 72, 985. https://doi.org/10.1130/0016-7606(1961)72[985:ESOSFI]2.0.CO;2

Dong, J.-J., Tu, C.-H., Lee, W.-R., Jheng, Y.-J., 2012. Effects of hydraulic conductivity/strength anisotropy on the stability of stratified, poorly cemented rock slopes. Computers and Geotechnics 40, 147–159. https://doi.org/10.1016/j.compgeo.2011.11.001

Fu, P., Dafalias, Y.F., 2011. Study of anisotropic shear strength of granular materials using DEM simulation. Int. J. Numer. Anal. Meth. Geomech. 35, 1098–1126. https://doi.org/10.1002/nag.945

Gischig, V., Preisig, G., Eberhardt, E., 2016. Numerical Investigation of Seismically Induced Rock Mass Fatigue as a Mechanism Contributing to the Progressive Failure of Deep-Seated Landslides. Rock Mech Rock Eng 49, 2457–2478. https://doi.org/10.1007/s00603-015-0821-z

Glade, T., Anderson, M.G., Crozier, M.J., 2005. Landslide hazard and risk. Wiley Online Library.

Glastonbury, J., Fell, R., 2010. Geotechnical characteristics of large rapid rock slides. Can. Geotech. J. 47, 116–132. https://doi.org/10.1139/T09-080

Goodman, R.E., Bray, J.W., 1976. Toppling of rock slopes. Presented at the Proc. Specialty Conf. on Rock Engineering for Foundations and Slopes, Amer. Soc. Civil Eng., pp. 201–234.

Grelle, G., Revellino, P., Donnarumma, A., Guadagno, F.M., 2011. Bedding control on landslides: a methodological approach for computer-aided mapping analysis. Nat. Hazards Earth Syst. Sci. 11, 1395–1409. https://doi.org/10.5194/nhess-11-1395-2011

Hawker, L., Neal, J., 2021. FABDEM V1-0. https://doi.org/10.5523/bris.25wfy0f9ukoge2gs7a5mqpq2j7

Hoek, E., 1964. Fracture of anisotropic rock. Journal of the Southern African Institute of Mining and Metallurgy 64, 501–518.

Hoek, E., Carranza-Torres, C., Corkum, B., 2002. Hoek-Brown failure criterion-2002 edition. Proceedings of NARMS-Tac 1, 267–273.

Hoek, E., Diederichs, M.S., 2006. Empirical estimation of rock mass modulus. International Journal of Rock Mechanics and Mining Sciences 43, 203–215. https://doi.org/10.1016/j.ijrmms.2005.06.005

Huggel, C., Clague, J.J., Korup, O., 2012. Is climate change responsible for changing landslide activity in high mountains? Earth Surface Processes and Landforms 37, 77–91. https://doi.org/10.1002/esp.2223

Hungr, O., Leroueil, S., Picarelli, L., 2014. The Varnes classification of landslide types, an update. Landslides 11, 167–194. https://doi.org/10.1007/s10346-013-0436-y

Iverson, R.M., Reid, M.E., 1992. Gravity-driven groundwater flow and slope failure potential: 1. Elastic Effective-Stress Model. Water Resour. Res. 28, 925–938. https://doi.org/10.1029/91WR02694

Jaboyedoff, M., Crosta, G.B., Stead, D., 2011. Slope tectonics: a short introduction. SP 351, 1–10. https://doi.org/10.1144/SP351.1

Jaeger, J.C., Cook, N.G.W., Zimmerman, R.W., 2007. Fundamentals of rock mechanics, 4th ed. ed. Blackwell Pub, Malden, MA.

Katz, O., Morgan, J.K., Aharonov, E., Dugan, B., 2014. Controls on the size and geometry of landslides: Insights from discrete element numerical simulations. Geomorphology 220, 104–113. https://doi.org/10.1016/j.geomorph.2014.05.021

Korup, O., Densmore, A.L., Schlunegger, F., 2010. The role of landslides in mountain range evolution. Geomorphology 120, 77–90. https://doi.org/10.1016/j.geomorph.2009.09.017

Lacroix, P., Handwerger, A.L., Bièvre, G., 2020. Life and death of slow-moving landslides. Nat Rev Earth Environ 1, 404–419. https://doi.org/10.1038/s43017-020-0072-8

Lavé, J., Guérin, C., Valla, P.G., Guillou, V., Rigaudier, T., Benedetti, L., France-Lanord, C., Gajurel, A.P., Morin, G., Dumoulin, J.P., Moreau, C., Galy, V., 2023. Medieval demise of a Himalayan giant summit induced by mega-landslide. Nature 619, 94–101. https://doi.org/10.1038/s41586-023-06040-5

Leshchinsky, D., Baker, R., Silver, M.L., 1985. Three dimensional analysis of slope stability. Int. J. Numer. Anal. Methods Geomech. 9, 199–223. https://doi.org/10.1002/nag.1610090302

Li, X., Wartman, J., Tang, H., Yan, J., Luo, H., Hu, W., 2014. Dynamic Centrifuge Modelling Tests for Sliding Rock Slopes, in: Sassa, K., Canuti, P., Yin, Y. (Eds.), Landslide Science for a Safer Geoenvironment. Springer International Publishing, Cham, pp. 75–79. https://doi.org/10.1007/978-3-319-05050-8_13

Marc, O., Behling, R., Andermann, C., Turowski, J.M., Illien, L., Roessner, S., Hovius, N., 2019. Long-term erosion of the Nepal Himalayas by bedrock landsliding: the role of monsoons, earthquakes and giant landslides. Earth Surface Dynamics 7, 107–128. https://doi.org/10.5194/esurf-7-107-2019

Marinos, P., Hoek, E., 2000. GSI: a geologically friendly tool for rock mass strength estimation. Presented at the ISRM international symposium, ISRM, p. ISRM-IS.

Marinos, Vassilis., Carter, Trevor.G., 2018. Maintaining geological reality in application of GSI for design of engineering structures in rock. Engineering Geology 239, 282–297. https://doi.org/10.1016/j.enggeo.2018.03.022

McLamore, R., Gray, K.E., 1967. The Mechanical Behavior of Anisotropic Sedimentary Rocks. Journal of Engineering for Industry 89, 62–73. https://doi.org/10.1115/1.3610013

Moon, S., Perron, J.T., Martel, S.J., Holbrook, W.S., St. Clair, J., 2017. A model of three-dimensional topographic stresses with implications for bedrock fractures, surface processes, and landscape evolution: Three-Dimensional Topographic Stress. J. Geophys. Res. Earth Surf. 122, 823–846. https://doi.org/10.1002/2016JF004155

Munjiza, A.A., 2004. The combined finite-discrete element method. John Wiley & Sons.

Nasseri, M.H.B., Rao, K.S., Ramamurthy, T., 2003. Anisotropic strength and deformational behavior of Himalayan schists. International Journal of Rock Mechanics and Mining Sciences 40, 3–23. https://doi.org/10.1016/S1365-1609(02)00103-X

Niandou', H., Shaoi, J.F., HENRYf, J.P., Fourmaintraux, D., 1997. Laboratory Investigation of the Behaviour of Tournemire Shale. Int. J. Rock Mech. Min. Sci. 34, 3–16.

Parsons, A.J., Law, R.D., Searle, M.P., Phillips, R.J., Lloyd, G.E., 2016. Geology of the Dhaulagiri-Annapurna-Manaslu Himalaya, Western Region, Nepal. 1:200,000. Journal of Maps 12, 100–110. https://doi.org/10.1080/17445647.2014.984784

Petley, D.N., Higuchi, T., Petley, D.J., Bulmer, M.H., Carey, J., 2005. Development of progressive landslide failure in cohesive materials. Geol 33, 201. https://doi.org/10.1130/G21147.1

Read, J., Stacey, P. (Eds.), 2009. Guidelines for open pit slope design, Reprint. with corr. ed. CSIRO Publ. [u.a.], Collingwood, Vic.

Roy, S., Baruah, A., Misra, S., Mandal, N., 2015. Effects of bedrock anisotropy on hillslope failure in the Darjeeling-Sikkim Himalaya: an insight from physical and numerical models. Landslides 12, 927–941. https://doi.org/10.1007/s10346-014-0513-x

Saroglou, H., Marinos, P., Tsiambaos, G., 2004. The anisotropic nature of selected metamorphic rocks from Greece. Journal of the Southern African Institute of Mining and Metallurgy 104, 217–222. https://doi.org/10.10520/AJA0038223X_2825

Schmidt, K.M., Montgomery, D.R., 1995. Limits to Relief. Science 270, 617–620. https://doi.org/10.1126/science.270.5236.617

Scholtès, L., Donzé, F.V., 2015. A DEM analysis of step-path failure in jointed rock slopes. Comptes Rendus Mécanique 343, 155–165. https://doi.org/10.1016/j.crme.2014.11.002

Scholtès, L., Donzé, F.-V., 2013. A DEM model for soft and hard rocks: Role of grain interlocking on strength. Journal of the Mechanics and Physics of Solids 61, 352–369. https://doi.org/10.1016/j.jmps.2012.10.005

Scholtès, L., Donzé, F.-V., 2012. Modelling progressive failure in fractured rock masses using a 3D discrete element method. International Journal of Rock Mechanics and Mining Sciences 52, 18–30. https://doi.org/10.1016/j.ijrmms.2012.02.009

Searle, M.P., 2010. Low-angle normal faults in the compressional Himalayan orogen; Evidence from the Annapurna–Dhaulagiri Himalaya, Nepal. Geosphere 6, 296–315. https://doi.org/10.1130/GES00549.1

Šmilauer, V., Angelidakis, V., Catalano, E., Caulk, R., Chareyre, B., Chèvremont, W., Dorofeenko, S., Duriez, J., Dyck, N., Elias, J., Er, B., Eulitz, A., Gladky, A., Guo, N., Jakob, C., Kneib, F., Kozicki, J., Marzougui, D., Maurin, R., Modenese, C., Pekmezi, G., Scholtès, L., Sibille, L., Stransky, J., Sweijen, T., Thoeni, K., Yuan, C., 2021. Yade documentation. The Yade Project. https://doi.org/10.5281/zenodo.5705394

Stead, D., Wolter, A., 2015. A critical review of rock slope failure mechanisms: The importance of structural geology. Journal of Structural Geology 74, 1–23. https://doi.org/10.1016/j.jsg.2015.02.002

Stockton, E., Leshchinsky, B.A., Olsen, M.J., Evans, T.M., 2019. Influence of both anisotropic friction and cohesion on the formation of tension cracks and stability of slopes. Engineering Geology 249, 31–44. https://doi.org/10.1016/j.enggeo.2018.12.016

Sun, L., Grasselli, G., Liu, Q., Tang, X., Abdelaziz, A., 2022. The role of discontinuities in rock slope stability: Insights from a combined finite-discrete element simulation. Computers and Geotechnics 147, 104788. https://doi.org/10.1016/j.compgeo.2022.104788

Teshebaeva, K., Echtler, H., Bookhagen, B., Strecker, M., 2019. Deep-seated gravitational slope deformation (DSGSD) and slow-moving landslides in the southern Tien Shan Mountains: new insights from InSAR, tectonic and geomorphic analysis. Earth Surf. Process. Landforms 44, 2333–2348. https://doi.org/10.1002/esp.4648

Thouret, J.-C., 1983. Géodynamique des grands versants de l’Ankhu Khola, Népal central. Editions du Centre national de la recherche scientifique.

Tien, Y.M., Kuo, M.C., Juang, C.H., 2006. An experimental investigation of the failure mechanism of simulated transversely isotropic rocks. International Journal of Rock Mechanics and Mining Sciences 43, 1163–1181. https://doi.org/10.1016/j.ijrmms.2006.03.011

Tong, Z., Fu, P., Zhou, S., Dafalias, Y.F., 2014. Experimental investigation of shear strength of sands with inherent fabric anisotropy. Acta Geotech. 9, 257–275. https://doi.org/10.1007/s11440-014-0303-6

Townsend, K.F., Gallen, S.F., Clark, M.K., 2020. Quantifying Near-Surface Rock Strength on a Regional Scale From Hillslope Stability Models. Journal of Geophysical Research: Earth Surface 125, e2020JF005665. https://doi.org/10.1029/2020JF005665

Uhlir, C., Schramm, J.-M., 1997. Weathering and erosional processes within the landslide deposit of Jarlang (Ganesh Himal, central Nepal). Journal of Nepal Geological Society 53–65.

Utili, S., Crosta, G.B., 2011. Modeling the evolution of natural cliffs subject to weathering: 2. Discrete element approach. J. Geophys. Res. 116, n/a-n/a. https://doi.org/10.1029/2009JF001559

Viles, H.A., 2013. Linking weathering and rock slope instability: non-linear perspectives: Linking weathering and rock slope instability. Earth Surf. Process. Landforms 38, 62–70. https://doi.org/10.1002/esp.3294Wang, C., Tannant, D.D., Lilly, P.A., 2003. Numerical analysis of the stability of heavily jointed rock slopes using PFC2D. International Journal of Rock Mechanics and Mining Sciences 40, 415–424. https://doi.org/10.1016/S1365-1609(03)00004-2

Wang, P., Yang, T., Zhou, J., 2018. Slope failure analysis considering anisotropic characteristics of foliated rock masses. Arab J Geosci 11, 222. https://doi.org/10.1007/s12517-018-3583-6

Yang, C.-M., Kang, K.-H., Yang, S.-H., Li, K.-W., Wang, H.-J., Lee, Y.-T., Lin, K.-K., Pan, Y.-W., Liao, J.-J., 2020. Large paleo-rockslide induced by buckling failure at Jiasian in Southern Taiwan. Landslides 17, 1319–1335. https://doi.org/10.1007/s10346-020-01360-3

Zheng, Y., Chen, C., Liu, T., Zhang, H., Xia, K., Liu, F., 2018. Study on the mechanisms of flexural toppling failure in anti-inclined rock slopes using numerical and limit equilibrium models. Engineering Geology 237, 116–128. https://doi.org/10.1016/j.enggeo.2018.02.006

Zheng, Y., Wang, R., Chen, C., Meng, F., 2021. Analysis of Flexural Toppling Failure in Rock Slopes Using Discrete Element Method. Front. Earth Sci. 9, 773088. https://doi.org/10.3389/feart.2021.773088

Zou, Z., Tang, H., Xiong, C., Su, A., Criss, R.E., 2017. Kinetic characteristics of debris flows as exemplified by field investigations and discrete element simulation of the catastrophic Jiweishan rockslide, China. Geomorphology 295, 1–15. https://doi.org/10.1016/j.geomorph.2017.06.012